Chapter 3

PREDICTING GLYCOSAMINOGLYCAN-SURFACE PROTEIN INTERACTIONS: IMPLICATIONS FOR STUDYING AXONAL GROWTH

Adam R. Griffith,[a,b,1] Claude J. Rogers,[b,c,1] Ravinder Abrol,[a,b] William A. Goddard III[a,ab,*]
Greg Miller,[b,c] and Linda C. Hsieh-Wilson,[b,c]
[a]Materials and Process Simulation Center,
California Institute of Technology, Pasadena, CA 91125
[b]Division of Chemistry and Chemical Engineering
California Institute of Technology, Pasadena, CA 91125,
[c]Howard Hughes Medical Institute,
[1]These two authors contributed equally
[*]To whom correspondence should be addressed; email wag@wag.caltech.edu

Abstract

Glycosaminoglycan (GAG)-protein interactions play important roles in the development and maintenance of the nervous system, angiogenesis, spinal cord injury, viral invasion, and immune response. Unfortunately, little structural information is available for these complexes; indeed, for such important GAGs as the highly sulfated chondroitin sulfate motifs, CS-E and CS-D, there are no structural data. This is due to the structural heterogeneity of GAGs and the difficulty of obtaining sufficient quantities of material of consistent length and sulfation pattern. Here, we describe the development and validation of the GAG-Dock computational method to accurately predict the binding poses of protein-bound GAGs. We validate that GAG-Dock accurately reproduces (< 1 Å RMSD) the crystal structure poses for four known heparin-protein structures. Further, we predict the pose of heparin and chondroitin sulfate derivatives bound to the axonal guidance proteins: protein tyrosine phosphatase σ (RPTPσ) and the Nogo receptor (NgR). Such predictions should be useful in understanding and interpreting the role of GAGs in axonal growth and other processes.

Keywords: docking | chondroitin sulfate | heparin | RPTPσ | NgR | axonal growth

Abbreviations: CS, chondroitin sulfate, GAG, glycosaminoglycan; HS, heparin sulfate; LRR, leucine-rich repeat; RMSD, root-mean-square deviation

Introduction

The glycosaminoglycans (GAGs) heparin sulfate (HS) and chondroitin sulfate (CS) are involved in a diverse array of physiological processes, such as cell proliferation, migration, differentiation, morphogenesis, angiogenesis, blood coagulation, axon guidance, and spinal cord injury through interactions with a wide variety of proteins (1-4). Despite the importance of GAG-protein interactions, there is remarkably little structural information for these complexes. This is due in part to the inherent heterogeneity of GAGs both in length and degree of sulfation, and the lack of tools required to obtain homogeneous oligosaccharides. GAGs form a family of linear polysaccharides composed of alternating uronic acid and hexosamine units. The polysaccharides can vary in length, net charge, disaccharide composition, and the pattern and degree of sulfation. The biosynthesis leads to distinct sulfation motifs for both CS and HS (Fig. 3-1). Recent studies have shown that biological activity is often dependent on the sulfation sequence, with specific, highly sulfated sequences directing the interactions of GAGs with growth factors and other signaling proteins (5-11).
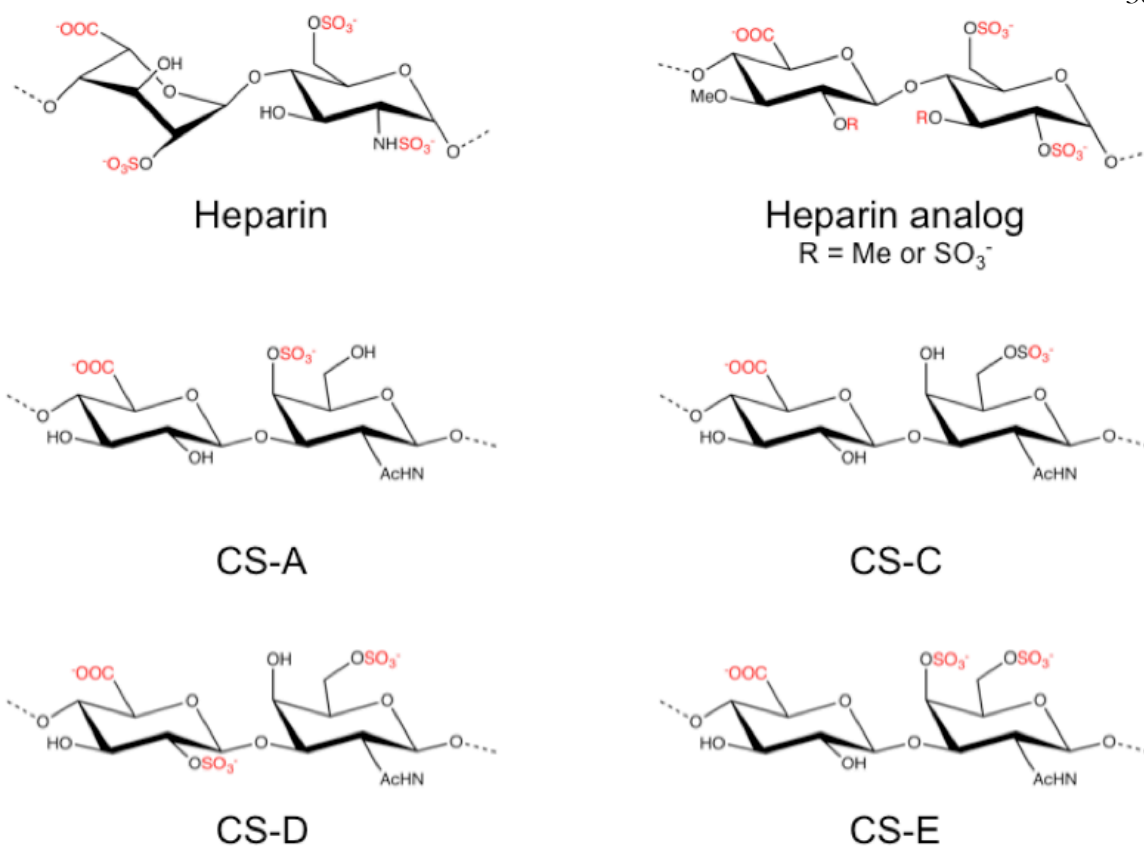
Figure 3-1 – Structures of glycosaminoglycans: heparin, heparin analog, chondroitin sulfates CS-A, CS-C, CS-D, and CS-E

Obtaining oligosaccharides with defined length and sulfation sequence is a difficult and specialized task for highly sulfated HS/heparin, and even more difficult with over-sulfated CS motifs such as CS-D and CS-E. As a result, structural data is available for only a handful of heparin-protein complexes, and no structural information is available for the CS-D and CS-E motifs. Recent work has shown that over-sulfated CS and HS interact directly with transmembrane receptors such as Nogo receptor (NgR) and type IIa receptor protein tyrosine phosphatase s (RPTPs) (11-14). However, it is unclear how GAGs engage and activate these receptors.

An alternative approach to *in vitro* structural determination is computational modeling of GAG-protein complexes. However, modeling GAG-protein interactions is extremely challenging because of the conformational flexibility of GAGs, the high charge density of GAGs and GAG-binding sites, and the weak surface complementarity of GAG-protein interactions. Despite these challenges, we (7) and others (15-18) have used molecular modeling successfully to predict the site at which GAGs engage their target proteins (7, 15-18). Some of these methods have limited accuracy in predicting the bound pose of the ligand or have limited robustness across different systems. Moreover, most of these methods have not been applied to systems other than the known heparin-protein structures.

Herein, we report the GAG-Dock method, that we developed to model accurately GAG-protein interactions, and we validate this method against known GAG-protein systems. We further apply the method to predict the protein-bound pose of various GAGs, including over-sulfated CS, to systems without known structures.

Summary of the GAG-Dock Method

Unlike small molecule ligands often docked successfully with various techniques (19-25, 44), even the truncated GAGs are large (the CS-A 4-mer has 60 heavy atoms and a net charge of -4; the CS-E 8-mer has 137 heavy atoms, a net charge of -12). Additionally, they bind to protein surfaces rather than in pockets, and engage proteins primarily through electrostatic interactions.

Our new GAG-Dock method is based on the DarwinDock and GenDock methodology (19, 20) with modifications to accommodate bulky, highly charged, surface-binding ligands

characteristic of GAGs. The GAG-binding site is generally not known; hence, it is necessary to examine systematically all possible binding regions. To do this, we complete two rounds of docking. First, we perform "coarse-level" docking to identify the best regions for further study. Second, we carry out "fine-level" docking on the best coarse regions to identify specific, strongly bound poses.

DarwinDock/GenDock

The DarwinDock/GenDock docking method applied here (19, 20) has been applied recently to predict ligand binding sites for GPCRs such as CB1 (21), GLP1-R (22), OR1G1 (23), TAS2R38 (42), AA_3R (24), and 5HT2b-R (25). Briefly it consists of four parts:

(1) <u>System Preparation.</u> Starting with target protein structures (usually with no hydrogen atoms), we prepare the systems as follows: (**a**) add hydrogens to various heavy atoms using standard bond distances and hydrogen binding criteria; (**b**) assign partial charges to all protein atoms based on general force field criteria and to all heteroatoms based on Mulliken charges; (**c**) optimize the protein structure using the force field to minimize the energy; (**d**) replace the 7 bulky, nonpolar residues (V/L/I/M/F/Y/W) with alanine ("alanization") to allow more complete sampling of the binding site; and (e) generate and select regions to be sampled by the ligand.

Generally the conformations of the protein side chains at the ligand binding site depend on the location and the conformation of the ligand (the pose), while the location and conformation of the ligand depends on the side chain conformations. Our solution to this "chicken-egg" problem is to alanize the bulky, nonpolar sidechains in step **d** (mentioned

above) to allow the ligand to fully sample available sites on the protein surface in the presence of the polar interactions. After selecting the best poses, the original nonpolar sidechains are replaced and reoptimized for each pose using SCREAM (45) in a process we call "dealanization". This allows a different set of protein side chains for each ligand pose.

To select poses that are close enough to the protein to interact favorably, while not too close to clash with protein atoms, we generate spheres to describe the space available for the ligand. This is done with the *sphgen* program (26), modified to work with protein surfaces. The spheres are partitioned into overlapping boxes ("sphere regions") for docking.

(2) Generation of a Complete Set of Poses. Prior to evaluating interaction energies between the ligand and protein, we want to sample the complete set of all possible poses. We do this by iteratively generating poses and then clustering them into Voronoi-like families using RMSD as the distance metric. This is done until the number of families stops changing as additional poses are added. For the cases considered here, we used an RMSD criterion of 2 Å in defining families, which generally leads to ~50,000 poses partitioned into ~2000 families, for each of which we select the "family head" as the central pose. During the pose-generation process no energies are calculated. To choose the best binding region, a quick but systematic "coarse" docking is first done using 10,000 poses without attempting the iterative, complete sampling.

(3) Scoring. To reduce computational cost, we want to minimize the number of poses for which an energy must be evaluated. Thus, scoring of the poses is broken into two steps.

First, the protein-ligand interaction energy of each family head is calculated, and the families ranked. Then, 90% of the families are eliminated based on the energy of the family head. Finally, the binding energies are calculated for all of the family members (children) in these 10% best families, and the poses are ranked with only the best 100 poses selected for further analysis. This hierarchical scoring procedure allows for a majority of the poses from the complete set (~50,000) to be eliminated without energy calculations.

(4) <u>Optimization and Refinement.</u> The 100 best poses from step 3 are further optimized and refined to identify the best poses. The first step is to de-alanize, i.e., replace and reoptimize the "alanized" residues with the full hydrophobic side chains. Simultaneously, all sidechains in the binding site are re-optimized (SCREAMed) using the SCREAM side-chain optimization method (45), in the presence of the specific ligand pose. Thus we end up with 100 different sets of side chain conformations, a different set for each ligand pose. Then, each of these 100 systems is energy minimized for 10 conjugate gradient steps. At this point the 100 poses are rescored and 50% eliminated. Then, another 50 steps of minimization are performed for these 50, with the poses again rescored. This final round of minimization is skipped during "coarse" docking.

GAG-Dock Modifications

The small-molecule docking methodology (DarwinDock/GenDock) was adapted to GAG structures through the following changes:

Sphere generation for flat protein surfaces requires alterations to the standard *sphgen* procedure (26). First, all spheres are generated with the 'dotlim' parameter in *sphgen* set to

-0.9, which allows spheres to be generated for flat surfaces. Second, in order to prevent the generation of deeply buried spheres that would be inaccessible to GAG ligands, a second set of spheres is generated using a probe radius of 2.8 Å instead of the normal 1.4 Å. The normal (1.4 Å probe radius) set of spheres is compared to the restricted (2.8 Å set), and only spheres within 2.8 Å of the restricted set sphere are kept. This procedure allows for spheres to be generated for the protein surface, while preventing those spheres from being so close to the surface to cause a large number of clashes with the protein during pose generation. These spheres are then partitioned into overlapping boxes/regions with 20 Å sides and 5 Å overlap.

System Preparation

All proteins studied here were prepared from PDB structures, with the exception of NgR1, NgR2, and NgR3, which required homology modeling from related systems with x-ray derived structures.

GAG Ligand Preparation

For the four validation systems, a ligand was already present in the crystal structure.

For the three systems without x-ray structures, no specific binding site is known, and hence we selected ligand structures based on the isolated ligands. Thus, the CS-A, CS-D, and CS-E structures used for docking to the non-validation systems were based on a CS-A hexasaccharide crystal structure (28), while the heparin structures for docking to the non-validation systems are based on a heparin 18-mer NMR structure. For CS-A and heparin, it

was only necessary to extend or truncate the structure to the appropriate length. We prepared CS-D and CS-E by extending the CS-A structure to a 12-mer, modifying the sulfation pattern, optimizing the sidechains, and performing Molecular Dynamics (MD) in solution. The structure closest to the average during MD was selected as the conformation for docking. This conformation was then truncated to a hexa- or octasaccharide by removing sugars from both the reducing and non-reducing ends. This step was necessary because the terminal saccharides display high variability in torsion angles during MD that are unphysical (inconsistent with possible movements) for an extended polysaccharide. Heparin and the other GAGs adopt a helical conformation that distributes charge radially along the length of the polysaccharide (31-33).

Results and Discussion

In order to validate the GAG-Dock method for such complex ligands and binding sites, we applied it to two sets of systems. The first set consists of the four validation systems for which a crystal structure including the ligand bound to the specific binding site was known. The second set of systems consists of three proteins known to bind to one or more GAG ligands, but for which the specific binding site was not known (although the general region of binding may be known). In each case, we followed the procedure of (1) coarse docking to identify the best regions, and (2) fine docking to identify the best ligand poses. In both cases the predicted binding energy was the criterion for selection.

Case 1: Validation of systems for which there are x-ray structures of the co-crystal

Five heparin-protein crystal structures have been solved, providing a means to validate our method. We applied GAG-Dock to four of these cases. We did not consider the 5th system, FGF1-FGFR2 (PDB: 1E0O (29)), because this 10-mer ligand is significantly more demanding computationally, but similar otherwise to the other validation cases. The RMSD comparisons for the predicted and crystal ligands for the validation systems are summarized in Table 3-1, showing that GAG-Dock reproduces the ligand positions with good accuracy. Figure S3-13 compares the nonbond interactions between the ligands and sidechains within the binding sites of the validation systems. As can be clearly seen from the plots in Fig. S3-13, most of the ligand-sidechain interactions were faithfully reproduced. A major source of error in the sidechain placement and interaction energies was the lack of waters in our validation systems. For structures without known binding sites, such as RPTPs and NgR, the placement of waters in an apo-protein crystal structure cannot be assumed to be correct for a ligand-bound structure, and even that information is lacking if homology modeling is used to generate the protein structure. Therefore, for a realistic assessment of the validation systems, any waters present in the crystal structures were removed. As waters often play a role in ligand binding, removing the waters allows sidechains in the protein to interact more strongly with the ligand.

FGF1

We validated our method using the crystal structure of the heparin hexasaccharide bound to two molecules of fibroblast growth factor 1 (FGF1, PDB: 2AXM (30)).

GAG-Dock correctly identified the binding site, with both molecules of FGF1 interacting with heparin at the same site, but with different specific residues interacting with the ligand for the proteins. The lowest-energy pose was within 0.70 Å root-mean-square deviation (RMSD) of the crystal structure ligand (Fig. 3-2A, S3-5, S3-6), calculated by comparing all atoms in the docked ligand to all atoms (including added hydrogen atoms) in the x-ray ligand.

Since the crystal structure is available, we docked the protein with all side chains in their experimental conformation. In this case we predict the lowest energy (strongest binding) ligand pose to have an RMSD error of 0.70 Å. Optimizing the residues for the heparin-binding site of the FGF1 molecules led to the lowest energy structure with an RMSD of 2.08 Å for the sidechains compared to the x-ray structure (Fig. S3-5). We consider that this is a success. Comparing to the x-ray pose, we find some minor differences in the energy contributions (Table S3-5). For example, K112 and K113 in chain A and K128 in chain B made stronger Coulomb and hydrogen bonding interactions with the ligand in the docked pose than in the x-ray (possibly because the water plays a role in the x-ray structure but not in ours). On the other hand, R119 was positioned farther from the ligand in the docked pose leading to weaker Coulomb interactions with the ligand. Overall the predicted energy contributions for the ligand interacting with each residue were consistent between the docked and crystal structures, indicating that these energy contributions can be used to understand the relative contributions to binding for each residue of the protein. Our conclusion is that our GAG-Dock methodology accurately predicts both the ligand pose and the relative importance of residues on the protein toward binding. Our analysis

suggests that K112, K113, K118, R122, and K128 make the most important contributions to heparin binding.

FGF2

For the complex of a heparin tetrasaccharide with FGF2 (PDB: 1BFB (34)), heparin makes contacts primarily with a single molecule of FGF2. However, in the crystal there are additional contacts with three nearby FGF2 molecules that appear to influence the conformation of the ligand. Thus, we docked the heparin tetrasaccharide to the central protein while including the three nearby FGFs to describe the conditions of the crystal structure. Again, GAG-Dock correctly predicts the binding site and the optimum pose of the crystal ligand (0.70 Å RMSD, Fig. 3-2B, S3-7).

For FGF2, the side chains of the active site differ from the x-ray structure by 2.09 Å RMSD. In particular, GAG-Dock predicts conformations of K120, R121, and K130 that lead to stronger hydrogen bond and Coulombic contributions to binding than in the x-ray structure (Table S3-6). However for FGF2, no residues had less favorable conformations in the docked structure compared to the crystal structure. Again, GAG-Dock correctly predicts the relative importance of all residues involved in binding, showing that residues K120, R121, K126, K130, and K136 contribute most strongly to heparin binding.

FGF2-FGFR1

Heparin is known to form a ternary complex with FGF and its receptor FGFR2. The crystal structure of the FGF2-FGFR1-heparin complex features a 2:2:2 stoichiometry (PDB: 1FQ9

(35)). In this structure, each heparin molecule (an 8-mer and a 6-mer) binds to the positively charged groove formed at the junction of the proteins, making contacts with an FGF2 molecule and with the D2 domains of both FGFR1 molecules. Interestingly, this structure is very similar to the FGF2-FGFR1 complex without heparin (0.37 Å RMSD (36)), suggesting that in this case GAG-Dock correctly predicts the multimeric protein-receptor-GAG complex (7). We docked both heparin molecules to regions near the FGF1 molecule and to both FGFR2 molecules. For both heparin molecules, the predicted pose correctly identifies the binding pose (with RMSD of 0.75 Å (8-mer) and 1.51 Å (6-mer); Fig. 3-2C, S3-8 – S3-11). The RMSD of the side chains in the binding site was 1.76 (8-mer) and 2.28 Å (6-mer). Again, the predicted pose accounts for the relative importance of residues involved in binding, leading to the same pharmacophore identified in the crystal structure (Table S3-7 – S3-11).

α-Antithrombin III

The interaction between heparin and α-antithrombin III (ATIII) is one of the most studied GAG-protein complexes due to its role in blood coagulation (37). The structure of ATIII bound to a heparin analog (PDB: 1E03 (38)) provided a more challenging test than the other validation cases. With no other protein species making significant contacts to the ligand, this structure lacked the constraints of the other validation systems. Even without such constraints, GAG-dock predicts the crystal structure pose with 0.60 Å RMSD (Fig. 3-2D, S3-12). The protein side chains in the binding site have an RMSD of 1.96 Å compared to the crystal structure. Again, our predicted pose accounts for the relative importance of

residues involved in binding, with residues R13 and K125 contributing more to binding
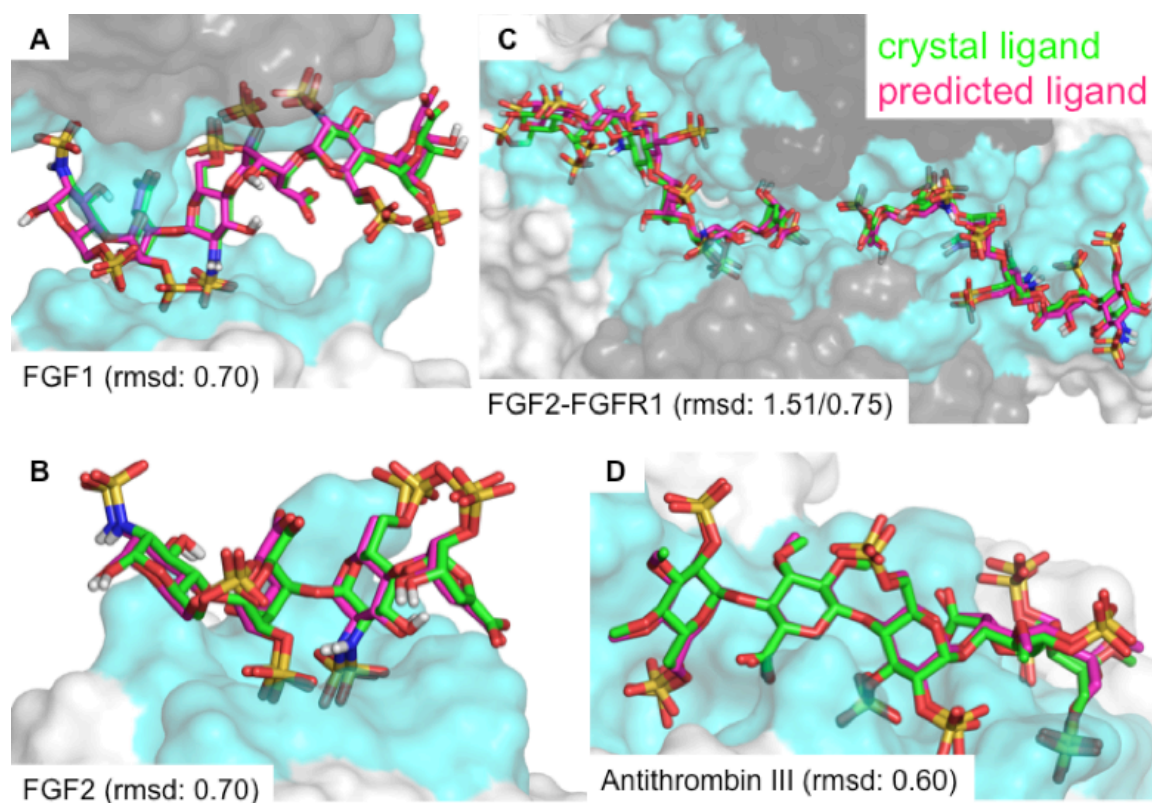
in the docked pose (Table S3-12).

Figure 3-2 – Comparison of predicted binding sites for heparin (magenta) to the x-ray crystal ligand positions. (A) FGF1 [RMSD: 0.70Å], (B) FGF2 [RMSD: 0.70Å], (C) FGF2-FGFR1 [RMSD: 1.51Å, 0.75Å], (D) α-antithrombin III [RMSD: 0.60Å]

Table 3-1 – Summary of docking validations. The resolution of the x-ray structure is given along with the heavy-atom RMSD between the predicted and x-ray position of the ligand.

	PDB	Resolution (Å)	RMSD* (Å)
FGF1	2AXM	3.00	0.70
FGF2	1BFB	1.90	0.70
FGF2-FGFR1 A	1FQ9	3.00	1.51
FGF2-FGFR1 B			0.75
α-ATIII	1EO3	2.90	0.60

*RMSD between docked and crystal structures

Case 2: Predictions for systems for which no co-crystal structure is available

Unlike heparin, no structural information is available for over-sulfated chondroitin sulfate motifs, despite increasing evidence of their biological importance (5, 7, 11, 12, 14). This is due to the difficulty in obtaining CS molecules that are purely one type (e.g. CS-E) for use in generating crystals. The recent identification of RPTPs and NgR as mediators of CS-induced axon inhibition, and the discovery that HS and CS have opposing effects on axon morphology (13), highlight the critical need for structural data to facilitate a mechanistic understanding of GAG function. Interestingly, both RPTPs and NgR bind to polysaccharides enriched in the CS-D, CS-E, or heparin sulfated epitopes, but not the lower sulfated motifs, such as CS-A. Thus, these proteins are ideal first systems to test how consistent our docking predictions are with *in vitro* binding data. To this end, we predicted docked structures of various GAGs to RPTPs, NgR1, NgR2, and NgR3.

RPTPs

While structural data for an RPTPs-GAG complex has not been reported, the GAG binding site on the protein is well understood. A defined GAG-binding site lies on the Ig1 domain of the protein, mediated by the K67, K68, K70, K71, R96, and R99 residues (13). This region forms a shallow electropositive cavity on the surface of the protein between b strands C-D and E-F (Fig. S3-14). The quadruple mutation of K67, K68, K70, K71 to alanine has been shown to impair binding to both CS and HS (12, 39). ELISA binding data to natural GAG polysaccharides indicate that RPTPs binds strongly to the CS-D and CS-E motifs and to heparin, but *not* to CS-A (11,14). To better understand RPTPs-GAG binding, we docked CS-E, CS-D, and heparin hexasaccharides to the protein (PDB: 2YD2). We also

docked CS-A hexasaccharide but did not find significant binding, which is consistent with the lack of binding observed experimentally. The docked CS-E and heparin structures are shown in Fig. 3-3, with detailed structures shown in Fig. S3-15 (CS-E) and S3-16 (heparin).

Indeed, GAG-Dock predicts that the GAG ligands bind to the previously identified GAG-binding site. That is, CS-E and heparin both bound to K67, K68, K71, N73, Q75, R76, R96, and R99 (Table S3-14). Additionally, CS-E made contacts with K71 and S74, and heparin made contacts with T97. Motifs with lower charge density, such as CS-A, had a poor docked scoring energy with the protein compared to CS-E and heparin, suggesting a weak interaction *in vitro*. A continuous tetrasaccharide makes contacts with RPTPs in the case of CS-E, while the entire heparin hexasaccharide makes contacts. These data are consistent with a single GAG-binding site; however, CS and HS have opposing effects on axon growth in DRG neuron cultures. HS promotes axonal growth whereas CS is growth inhibitory (13). This raises the question: How is it possible for these structurally related ligands to affect such drastically different signaling outcomes?

Based on size-exclusion chromatography coupled with multi-angle light scattering (SEC-MALS) using heparin fragments of various lengths and using a CS-A-enriched polysaccharide, Coles *et al.* (13) suggested that the difference between the glycans is that HS is capable of clustering RPTPs but CS is not. This is consistent with our GAG-Dock predictions (based on docked scoring energies). Later experimental studies demonstrated that CS-A has poor affinity to the protein compared to other CS sulfation motifs, especially

CS-E (11, 14). Unfortunately, CS-E oligosaccharides of suitable and defined length are not readily available to make the appropriate comparison. Nevertheless, it is plausible that CS-E polysaccharides should also be capable of simultaneously binding to multiple RPTPs molecules.

However, our docking data suggests another possibility. Because of the higher charge density and steeper helical twist of heparin/HS, our predicted pose for heparin hexasaccharide exposes several charged groups to the solvent. In contrast, the charged groups of CS-E are all engaged with the protein. Therefore, the mechanistic difference between heparin and CS-E may be that heparin is able to dimerize RPTPs, just as heparin does with FGFs, rather than merely clustering the receptor. Indeed, the SEC-MALS data in Coles *et al.* show that a decasaccharide is capable of binding two molecules of RPTPs, suggesting that bound heparin may be able to engage both proteins simultaneously (13).

A RPTPσ/CS-E
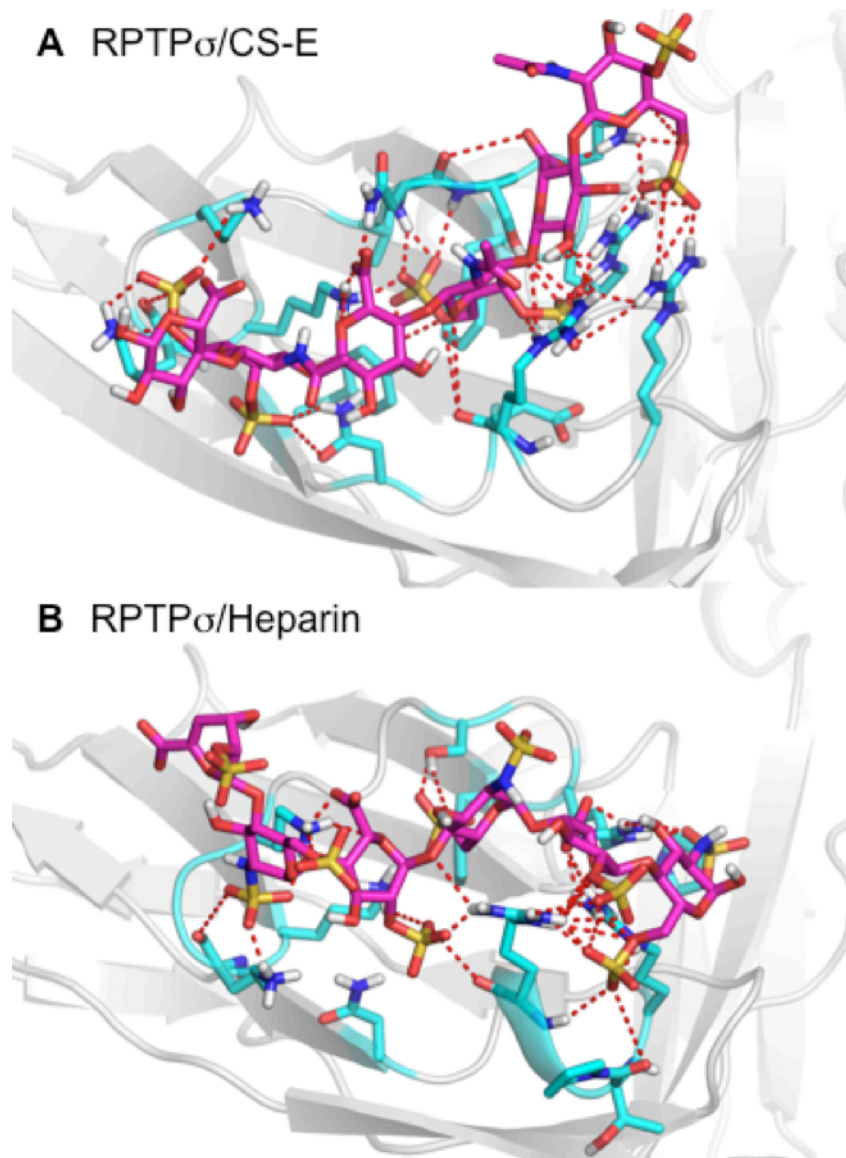
B RPTPσ/Heparin

Figure 3-3 – (A) CS-E and (B) heparin bound to RPTPs. Dotted lines indicate hydrogen bonds to the protein.

NgR

The NgRs are myelin-associated inhibitors that restrict axonal growth after injury. A recent study demonstrated that NgR1 and NgR3, but not NgR2, are involved in GAG-induced axonal inhibition (14). NgRs are comprised of 8.5 leucine-rich repeat (LRR) domains

flanked by N-terminal and C-Terminal LRR capping domains and a C-terminal stalk that

connects the protein to the membrane via a glycosylphosphatidylinositol (GPI) anchor (40).

Compared to RPTPs, less information is known about how NgR binds to GAGs; however,

domain deletion studies suggest that the C-terminal capping domain and stalk are required

for CS binding (14). C-terminal regions of NgR, such as the stalk, have not been resolved

in the reported crystal structures of the protein (41, 42).

To better understand the role of the C-terminal domains, we generated homology models of

NgR isoforms using the ROSETTA software (43). We carried out 5 ns of MD in the

presence of explicit water and counter ions to allow the 5 models per isoform to relax. We

then selected the structure nearest to the average conformation for each model, minimized

it, and then selected the lowest energy structure for each isoform to use in further studies.

The electrostatic potential surfaces of these homology models of the extracellular domain

of NgR isoforms 1–3 suggest an electrostatic basis for the difference in activity between

NgR2 and NgRs 1 and 3 (Fig. S3-17). Unlike the GAG-binding isoforms, NgR2 lacks

significant regions of electropositive potential. Our predicted binding energies from coarse-

level docking with a CS-E tetrasaccharide to NgR2 led to much weaker interactions (–

297.67 kcal/mol), relative to NgR1 and 3 (–641.27 and –985.46 kcal/mol, respectively),

consistent with experimental findings.

Based on fine-level docking with CS-A, -D, -E, and heparin hexasaccharides, followed by

5 ns MD relaxation in a full water box with counterions, we predict that GAGs bind to

regions of electropositive potential on the C-terminal cap of both NgR1 and NgR3 (Fig. 3-

4, S3-18, S3-23). GAG-Dock studies predict that the GAG-binding domains of NgR1 and NgR3 are on different faces of the C-terminal cap, although this could be due to the structural flexibility of this region of the protein and to discrepancies between the model and the natural state of the protein. We predict that the GAGs make polar or electrostatic contacts with residues R399, R414, R415, R416, R421, K422, R424, R426, and R430 on NgR1 (Table S3-15) and with residues R346, R350, K354, N355, N358, R360, K364, K399, R400, K401, K403 and R406 on NgR3 (Table S3-16). Many of these residues, particularly residues 414–426 on NgR1 and 399–406 on NgR3, were shown by mutagenesis studies to be important for GAG binding (14). Together, these results validate that GAG-Dock can be used both to understand the structural basis for extreme differences in GAG-binding activity between related proteins and to identify reliably the pharmacophore even in cases where the protein structure is ill defined. Detailed structures for CS-A, CS-D, CS-E, and heparin bound to NgR1 are shown in Fig. S3-19 – S3-22. Detailed structures for those ligand bound to NgR3 are shown in Fig. S3-24 – S3-27.
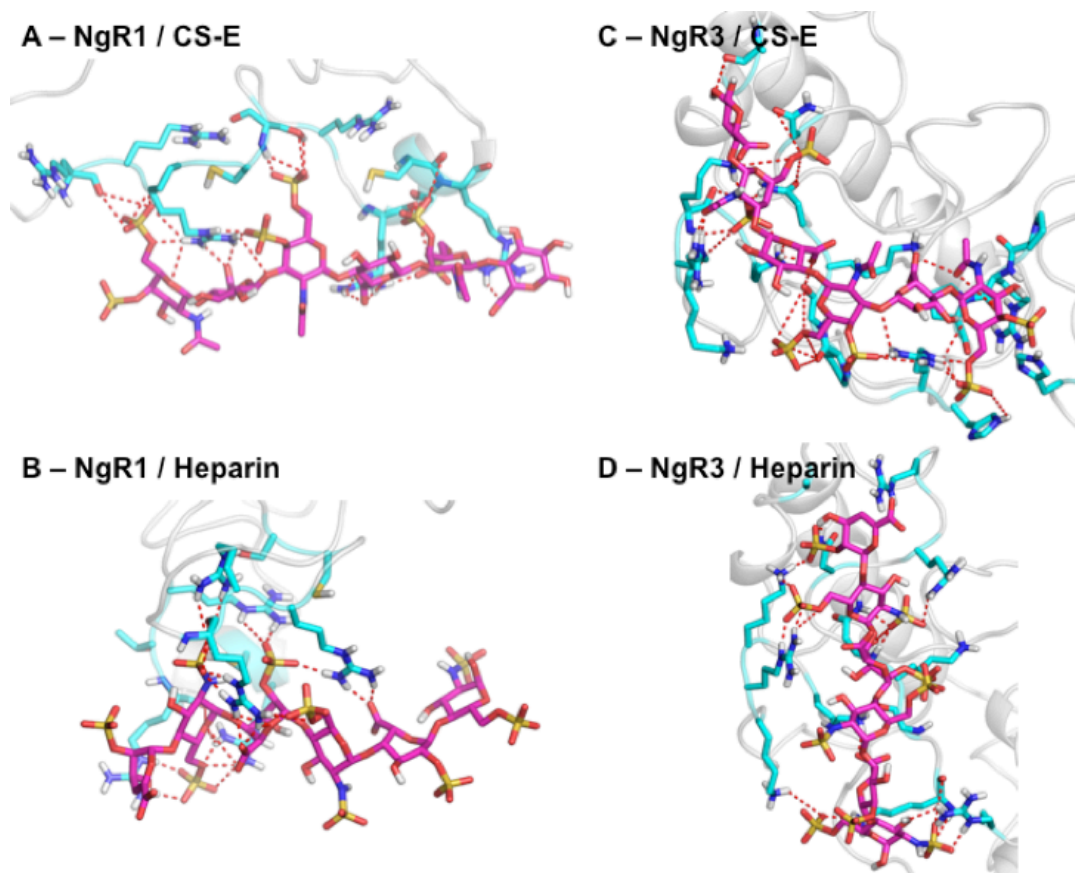
Figure 3-4 – (A) CS-E and (B) heparin bound to NgR1. (C) CS-E and (D) heparin bound to NgR3.

Suggested Post-Prediction Validations

Experimental validation of our novel RPTPs and NgR binding sites may be possible via mutation experiments. We carried out *in silico* mutations for our predicted CS-A, CS-D, CS-E, and heparin binding sites for RPTPs, NgR1, and NgR3 in order to identify reasonable suggestions for experimental validation. Rather than the more common alanine mutations, we employed a more subtle mutation to asparagine or glutamine. As noted above, the key interactions between the GAG ligands and the proteins involve arginines and lysines. Mutation of these residues to alanine represents a drastic change in character

and could result in significant disruption of the system beyond affecting binding. Mutation to asparagine or glutamine allows the possibility of maintaining some polar contact with the ligand, but without the benefit of strong charged interactions. Additionally, while the standard method is to identify mutations that decrease binding, we consider this approach to be ambiguous, as binding can be lost for many reasons. Therefore, in addition to the standard loss-of-binding mutations, we identified mutations that could potentially increase binding of the ligand to the protein.

We first employed single-residue mutations of all residues within the binding sites to either asparagine or glutamine while simultaneously optimizing the remaining sidechain conformations in the binding site using SCREAM, followed by 50 steps of conjugate gradient energy minimization. From these calculations we identified mutations that either resulted in additional or lost hydrogen bonding to the ligands. Based on these individual mutations, sets of mutations to either increase or decrease ligand binding were identified for each ligand/protein combination. It should be noted that some mutations of arginine or lysine may result in increased hydrogen bonding if the arginine or lysine was initially too constrained to make a hydrogen bond to the ligand. However, such a mutation still remains a net loss of overall binding energy due to the lost Coulomb interactions. Therefore, we only considered mutations of arginine or lysine to asparagine or glutamine for our loss-of-binding mutation sets.

For RPTPs we identified three sets of mutations that increased binding to CS-A, CS-D, or CS-E, but interestingly not to heparin. It is possible that RPTPs is already optimized for

heparin binding, but not for CS binding. Mutation set "G1" is specific for CS-E, while

"G2" is specific for CS-D, and "G3" is nonspecific with the exception of decreasing

heparin binding. Based on the single residue mutations we generated four sets of mutations

to decrease binding. As all of these mutations affect the key arginine and lysine residues,

they all unsurprisingly result in significant reductions in binding energy. The mutation sets

for RPTPs are summarized in Table 3-2, and the single mutations are summarized in Table

S3-17.

Table 3-2 – Predicted sets of mutations to either increase (left) or decrease (right) binding of ligands to RPTPs. Note that none of the sets show improved binding for heparin. Changes in binding energy are shown relative to the wildtype structures in both absolute change (kcal/mol) and in terms of percent change.

PTPS - Increased Binding (Relative Energy)				
Set	CSA	CSD	CSE	HEP	Mutations
G1	-1.7	-0.3	-34.2	30.5	V73N S75N Q76N F78Q
G2		-6.2	-35.0	12.6	29.7	N74Q S75N
G3	-17.8	-23.8	-29.0	21.2	V73Q S75N Q76N F78N N103Q

PTPS - Loss of Binding (Relative Energy)				
Set	CSA	CSD	CSE	HEP	Mutations
L1	565.5	719.2	709.8	1059.6	K68Q K69N K71Q R77N R97N R100N
L2	386.0	528.2	481.5	705.1	K71N R77Q R97N R100Q
L3	383.5	472.6	458.7	657.3	K68N K69Q R77N R100N
L4	468.6	629.7	603.3	891.1	K68N K71Q R77N R97N R100Q

PTPS - Increased Binding (Percent Change)				
Set	CSA	CSD	CSE	HEP	Mutations
G1	0.3	0.0	4.2	-2.9	V73N S75N Q76N F78Q
G2	1.1	4.5	-1.6	-2.8	N74Q S75N
G3	3.1	3.1	3.6	-2.0	V73Q S75N Q76N F78N N103Q

PTPS - Loss of Binding (Percent Change)				
Set	CSA	CSD	CSE	HEP	Mutations
L1	-97.3	-92.8	-87.8	-101.0	K68Q K69N K71Q R77N R97N R100N
L2	-66.4	-68.1	-59.6	-67.2	K71N R77Q R97N R100Q
L3	-66.0	-61.0	-56.7	-62.7	K68N K69Q R77N R100N
L4	-80.6	-81.2	-74.6	-84.9	K68N K71Q R77N R97N R100Q

For NgR1 we identified four sets of mutations to increase binding by building up from the

single mutation information. Surprisingly one of the mutation sets ("G3") did not show

any improvement in binding when tested. Set "G1" improved CS-A and CS-D binding, but

not CS-E or heparin. Set "G2" improved CS-D and heparin binding. Set "G4" improved

binding for every ligand except CS-E. It is again interesting that none of the mutation sets

improved CS-E binding. As with RPTPs, the four loss-of-binding mutation sets were all

effective in reducing ligand binding, but were non-specific for any ligand. The mutation

sets for NgR1 are summarized in Table 3-3, and single mutations are summarized in Table S3-18.

Table 3-3 – Predicted sets of mutations to either increase (left) or decrease (right) binding of ligands to NgR1. Note that none of the sets show improved binding for CS-E. Changes in binding energy are shown relative to the wildtype structures in both absolute change in binding energy (kcal/mol) and in terms of percent change.

NGR1 - Increased Binding (Relative Energy)				
Set	CSA	CSD	CSE	HEP	Mutations
G1	-15.8	-14.0	2.7	-3.6	C395Q C405N
G2	10.6	-30.8	4.2	-38.0	S396N N399Q C405N
G3	-0.1	0.4	10.5	-1.1	C395Q S396N S403Q C405Q
G4	-20.9	-19.6	9.8	-27.1	S396Q C405N

NGR1 - Decreased Binding (Relative Energy)				
Set	CSA	CSD	CSE	HEP	Mutations
L1	481.3	607.0	649.0	850.0	R390N R391N R392Q R402N R406N
L2	471.5	627.0	597.9	813.1	R390Q R391Q R400N R402N R406N
L3	382.4	463.0	580.7	610.0	R391N R392Q R402Q R406Q
L4	473.2	629.9	642.9	834.1	R390N R392Q R400N R402Q R406N

NGR1 - Increased Binding (Percent Change)				
Set	CSA	CSD	CSE	HEP	Mutations
G1	2.2	1.4	-0.3	0.3	C395Q C405N
G2	-1.5	3.1	-0.5	3.4	S396N N399Q C405N
G3	0.0	0.0	-1.2	0.1	C395Q S396N S403Q C405Q
G4	2.9	2.0	-1.1	2.4	S396Q C405N

NGR3 - Decreased Binding (Percent Change)				
Set	CSA	CSD	CSE	HEP	Mutations
L1	-65.3	-62.0	-71.3	-75.8	R390N R391N R392Q R402N R406N
L2	-64.0	-64.1	-65.7	-72.5	R390Q R391Q R400N R402N R406N
L3	-51.9	-47.3	-63.8	-54.4	R391N R392Q R402Q R406Q
L4	-64.2	-64.3	-70.6	-74.4	R390N R392Q R400N R402Q R406N

Each of the mutation sets to increase binding for NgR3 show improved binding to at least one of the ligands. None of the ligands is completely missed as heparin was for RPTPs or CS-E for NgR1. The mutation sets for NgR3 are summarized in Table 3-4, and single mutations are summarized in Table S3-19.

Table 3-4 – Predicted sets of mutations to either increase (left) or decrease (right) binding of ligands to NgR3. Changes in binding energy are shown relative to the wildtype structure in both absolute change (kcal/mol) and in terms of percent change.

NGR3 - Increased Binding (Relative Energy)					
Set	CSA	CSD	CSE	HEP	Mutations
G1	-15.9	6.9	-9.9	-10.1	I345Q A348N
G2	-3.1	0.8	-10.2	-0.1	I345Q
G3	-12.9	-5.1	-5.8	-12.2	A348N
G4	-7.7	1.9	7.9	-23.7	N338Q A348N

NGR3 - Decreased Binding (Relative Energy)					
Set	CSA	CSD	CSE	HEP	Mutations
L1	230.6	271.2	327.7	396.5	K331N K334Q R342N
L2	321.9	537.6	545.0	802.2	K331N R342N R380N R381N R383N
L3	470.9	771.7	858.4	1054.7	R330N K331N K334N R342N R380Q K381N K383N
L4	238.0	413.9	425.4	644.0	R340N R379N R380N R383N

NGR3 - Increased Binding (Percent Change)					
Set	CSA	CSD	CSE	HEP	Mutations
G1	2.2	-0.6	0.8	0.7	I345Q A348N
G2	0.4	-0.1	0.8	0.0	I345Q
G3	1.8	0.4	0.5	0.8	A348N
G4	1.0	-0.2	-0.6	1.5	N338Q A348N

NGR3 - Decreased Binding (Percent Change)					
Set	CSA	CSD	CSE	HEP	Mutations
L1	-31.3	-23.6	-27.0	-25.9	K331N K334Q R342N
L2	-43.7	-46.8	-44.9	-52.4	K331N R342N R380N R381N R383N
L3	-63.9	-67.1	-70.7	-68.9	R330N K331N K334N R342N R380Q K381N K383N
L4	-32.3	-36.0	-35.0	-42.1	R340N R379N R380N R383N

Conclusions

Predicting the binding sites of highly charged GAG ligands with multiple independent charge sites and numerous possible conformations seems a formidable challenge. The very large number of charged sites on the ligands and in the binding site likely leads to redistributions of the water and ions in the solvent making polarization likely of great importance. Nevertheless, we show for eight independent systems that the simple GAG-Dock modifications of the DarwinDock general docking approach accounts well for the enormous importance of electrostatic interactions, leading to plausible structures and relative binding energies that help distinguish the strength of binding for various GAG ligands to a wide variety of receptors likely to play essential roles in axonal growth. Given the difficulty of obtaining high quality co-crystals for x-ray studies, this simple GAG-Dock computational methodology may provide the best means for predicting the structure sufficiently accurately to help design experimental probes to elucidate the issues controlling axonal growth, perhaps suggesting modified ligands that might be more selective and controllable.

References

1. Capila I, Linhard RJ (2002) Heparin-protein interactions. *Angew Chem Int Ed* 41:390–412.

2. Raman R, Sasisekharan V, Sasisekharan R (2005) Structural insights into biological roles of protein-glycosaminoglycan interactions. *Chem Biol* 12:267–277.

3. Sugahara K et al. (2003) Recent advances in the structural biology of chondroitin sulfate and dermatan sulfate. *Curr Opin Struct Biol* 13:612–620.

4. Gama CI, Hsieh-Wilson LC (2005) Chemical approaches to deciphering the glycosaminoglycan code. *Curr Opin Chem Biol* 9:609–619.

5. Gama CI et al. (2006) Sulfation patterns of glycosaminoglycans encode molecular recognition and activity. *Nat Chem Biol* 2:467–473.

6. Shipp EL, Hsieh-Wilson LC (2007) Profiling the sulfation specificities of glycosaminoglycan interactions with growth factors and chemotactic proteins using microarrays. *Chem Biol* 14:195–208.

7. Rogers CJ et al. (2011) Elucidating glycosaminoglycan-protein-protein interactions using carbohydrate microarray and computational approaches. *Proc Natl Acad Sci USA* 108:9747–9752.

8. Hricovíni M et al. (2002) Active conformations of glycosaminoglycans. NMR determination of the conformation of heparin sequences complexed with antithrombin and fibroblast growth factors in solution. *Semin Thromb Hemost* 28:325–334.

9. Rusnati M et al. (1997) Interaction of HIV-1 Tat protein with heparin. Role of the backbone structure, sulfation, and size. *J Biol Chem* 272:11313–11320.

10. Kuschert GS et al. (1999) Glycosaminoglycans interact selectively with chemokines and modulate receptor binding and cellular responses. *Biochemistry* 38:12959–12968.

11. Brown JM et al. (2012) A sulfated carbohydrate epitope inhibits axon regeneration after injury. *Proc Natl Acad Sci USA*.

12. Shen Y et al. (2009) PTPσ is a receptor for chondroitin sulfate proteoglycan, an inhibitor of neural regeneration. *Science* 326:592–596.

13. Coles CH et al. (2011) Proteoglycan-specific molecular switch for RPTPσ clustering and neuronal extension. *Science* 332:484–488.

14. Dickendesher TL et al. (2012) NgR1 and NgR3 are receptors for chondroitin sulfate proteoglycans. *Nat Neurosci* 15:703–712.

15. Bitomsky W, Wade RC (1999) Docking of Glycosaminoglycans to Heparin-Binding Proteins: Validation for aFGF, bFGF, and Antithrombin and Application to IL-8. *J Am Chem Soc* 121:3004–3013.

16. Bytheway I, Cochran S (2004) Validation of molecular docking calculations involving FGF-1 and FGF-2. *J Med Chem* 47:1683–1693.

17. Forster M, Mulloy B (2006) Computational approaches to the identification of heparin-binding sites on the surfaces of proteins. *Biochem Soc Trans* 34:431–434.

18. Takaoka T, Mori K, Okimoto N, Neya S, Hoshino T (2007) Prediction of the Structure of Complexes Comprised of Proteins and Glycosaminoglycans Using Docking Simulation and Cluster Analysis. *J Chem Theory Comput* 3:2347–2356.

19. Cho AE et al. (2005) The MPSim-Dock hierarchical docking algorithm: application to the eight trypsin inhibitor cocrystals. *J Comput Chem* 26:48–71.

20. Floriano WB, Vaidehi N, Zamanakos G, Goddard WA (2004) HierVLS hierarchical docking protocol for virtual ligand screening of large-molecule databases. *J Med Chem* 47:56–71.

21. Scott CE, Abrol R, Ahn KH, Kendall DA, Goddard WA (2013) Molecular basis for dramatic changes in cannabinoid CB1 G protein-coupled receptor activation upon single and double point mutations. *Protein Sci* 22:101–113.

22. Kirkpatrick A, Heo J, Abrol R, Goddard WA (2012) Predicted structure of agonist-bound glucagon-like peptide 1 receptor, a class B G protein-coupled receptor. *Proc Natl Acad Sci USA* 109:19988–19993.

23. Charlier L et al. (2012) How broadly tuned olfactory receptors equally recognize their agonists. Human OR1G1 as a test case. *Cell Mol Life Sci* 69:4205–4213.

24. Kim S-K, Riley L, Abrol R, Jacobson KA, Goddard WA (2011) Predicted structures of agonist and antagonist bound complexes of adenosine A3 receptor. *Proteins* 79:1878–1897.

25. Kim S-K, Li Y, Abrol R, Heo J, Goddard WA (2011) Predicted structures and dynamics for agonists and antagonists bound to serotonin 5-HT2B and 5-HT2C receptors. *J Chem Inf Model* 51:420–433.

26. Moustakas DT et al. (2006) Development and validation of a modular, extensible

docking program: DOCK 5. *J Comput Aided Mol Des* 20:601–619.

27. Baker NA, Sept D, Joseph S, Holst MJ, McCammon JA (2001) Electrostatics of nanosystems: application to microtubules and the ribosome. *Proc Natl Acad Sci USA* 98:10037–10041.

28. Winter WT, Arnott S, Isaac DH (1978) Chondroitin 4-sulfate: The structure of a sulfated glycosaminoglycan. *J Mol Biol* 125:1–19.

29. Pellegrini L, Burke DF, Delft von F, Mulloy B, Blundell TL (2000) Crystal structure of fibroblast growth factor receptor ectodomain bound to ligand and heparin. *Nature* 407:1029–1034.

30. DiGabriele AD et al. (1998) Structure of a heparin-linked biologically active dimer of fibroblast growth factor : Abstract : Nature. *Nature* 393:812–817.

31. Tanaka K (1978) Physicochemical properties of chondroitin sulfate. I. Ion binding and secondary structure. *J Biochem* 83:647–653.

32. W D Comper OZ (1990) Hydrodynamic properties of connective-tissue polysaccharides. *Biochemical Journal* 269:561.

33. Khan S, Gor J, Mulloy B, Perkins SJ (2010) Semi-rigid solution structures of heparin by constrained X-ray scattering modelling: new insight into heparin-protein complexes. *J Mol Biol* 395:504–521.

34. Faham S, Hileman RE, Fromm JR, Linhardt RJ, Rees DC (1996) Heparin structure and interactions with basic fibroblast growth factor. *Science* 271:1116–1120.

35. Schlessinger J et al. (2000) Crystal structure of a ternary FGF-FGFR-heparin complex reveals a dual role for heparin in FGFR binding and dimerization. *Mol Cell* 6:743–750.

36. Plotnikov AN, Schlessinger J, Hubbard SR, Mohammadi M (1999) Structural basis for FGF receptor dimerization and activation. *Cell* 98:641–650.

37. Bourin MC, Lindahl U (1993) Glycosaminoglycans and the regulation of blood coagulation. *Biochem J* 289 (Pt 2):313–330.

38. McCoy AJ, Pei XY, Skinner R, Abrahams JP, Carrell RW (2003) Structure of beta-antithrombin and the effect of glycosylation on antithrombin's heparin affinity and activity. *J Mol Biol* 326:823–833.

39. Aricescu AR, McKinnell IW, Halfter W, Stoker AW (2002) Heparan sulfate proteoglycans are ligands for receptor protein tyrosine phosphatase σ. *Mol Cell Biol* 22:1881–1892.

40. Fournier AE, GrandPre T, Strittmatter SM (2001) Identification of a receptor mediating Nogo-66 inhibition of axonal regeneration. *Nature* 409:341–346.

41. Barton WA et al. (2003) Structure and axon outgrowth inhibitor binding of the Nogo-66 receptor and related proteins. *EMBO J* 22:3291–3302.

42. He XL et al. (2003) Structure of the Nogo Receptor EctodomainA Recognition

Module Implicated in Myelin Inhibition. *Neuron* 38:177–185.

43. Kim DE, Chivian D, Baker D (2004) Protein structure prediction and analysis using the Robetta server. *Nucleic Acids Res* 32:W526–31.

44. Lang PT, Brozell SR, Mukherjee S, Pettersen EF, Meng EC, Thomas V, Rizzo RC, Case DA, James TL, Kuntz ID. DOCK 6: combining techniques to model RNA-small molecule complexes. RNA. 2009 Jun;15(6):1219-30.

45. Kam, Victor Wai Tak (2008) *Methods in computational protein design.* Dissertation (Ph.D.), California Institute of Technology.

46. Mayo S.L., Olafson B.D., Goddard WA (1990) A Generic Force Field for Molecular Simulations. *J. Phys. Chem.* 94, 8897.

47. Lim K-T, Brunett S, Iotov M, McClurg RB, Vaidehi N, Dasgupta S, Taylor S, Goddard WA (1997) Molecular Dynamics for Very Large Systems on Massively Parallel Computers: The MPSim Program. *J. Comp. Chem.* 18, 501.

Jaguar, version 8.9, Schrödinger, LLC, New York, NY, 2015.

Supplementary Information

System Preparation

Crystal structures & PTPσ. Protein molecules within 5 Å of the GAG ligand, if present, were selected from the PDB. Hydrogen atoms were added with tleap (S23) and CHARMM (S1) charges were assigned to each atom. The system was minimized using the DREIDING force field (S2).

NgR. Five homology models for full-length NgR1, 2, and 3 were obtained using ROSETTA (S3). Each model was minimized (5000 steps) and allowed to relax in the presence of water and counterions with 5 ns of MD. MD was performed using NAMD in four steps, as described later in the MD section. Briefly, first, a water box bounding the protein was minimized with the protein kept fixed. Second, 0.5 ns of NPT MD were performed on the water box. Third, the entire systems were minimized. Finally, 5 ns of

NPT MD were performed on the entire system. For each initial conformation, the conformation closest to the average structure from the 5 ns MD was minimized and the lowest-energy conformation was selected for each isoform.

DarwinDock

The concept behind DarwinDock (S4-S12) is (1) to generate a complete set of poses for the binding site while minimizing the number of energy evaluations, (2) then to collect these into a smaller sets containing all poses likely to be important, (3) then to evaluate the binding energy of this relatively small set to find the best poses, while ensuring that no poses are missed that might prove to be important.

Pose generation is accomplished by iteratively generating poses (but no energies) using DOCK 6 (S13) and clustering them into families using our Closest-Neighbor Seeded clustering algorithm (described below). Our usage of DOCK 6 is very simplistic, utilizing only the bump filter. We follow the default settings for generating the bump grid for DOCK 6 and set the bump cutoff to 5. Two calls to DOCK 6 are generally made. First, a request for 40,000 poses is made to determine the approximate percentage of poses that will pass the DOCK bump filter. Then a second request for poses is made, based on the percent of poses passing the bump test so that enough poses are returned to be sufficient for the iterative completeness cycle. Initially the first 5000 poses are clustered with a 2 Å diversity, then the next 5000 poses are added and reclustered, leading an increased number of families. This process is continued in increments of 5000 poses until the number of new families represents less than 5% of the total number of families at that point.

Due to the computational difficulty of dealing with GAG ligands – which are considerably larger than normal small-molecule ligands for which DarwinDock was developed – leading to correspondingly increased search volumes, we restrict the number of poses during this iterative completeness cycle to 50,000. Furthermore, it is generally not possible to request more than 15 million poses (sometimes fewer) from DOCK6 before memory limitations intercede. As a result, most regions reach the 50,000 pose limit before reaching the 5% new families threshold. Other regions may fall well short of 50,000 poses due to their geometry and memory limitations.

After generating a complete set of poses, or the largest set within our computational limits, we score all family heads (generally ~2000). For each family the central pose (based on the RMSD) is denoted as the family head. The protein-ligand interaction energy of each family head is evaluated using the DREIDING forcefield (S2) with MPSim (S14). DREIDING partitions non-bond energies into Coulomb, hydrogen-bond, and Van Der Waals (VDW). For GAG-Dock the interaction energy is the sum of all ligand-protein Coulomb and hydrogen-bond energies plus 10% of the (VDW) energy. Including only 10% of the VDW energy allows for strong polar interactions with the protein with moderate clashes that can be resolved during sidechain optimization. Not including the VDW energy results in poses with severe, unresolvable clashes with the protein, while including the full VDW energy results in poses that are too far from the protein and make poor contact.

After evaluating the interaction energy for the family heads, we eliminate the worst 90% of the families. Next, we evaluate the interaction energy for all children in the remaining 10% of families. From these children we select best 100 based on binding energy. Eliminating

90% of the families without evaluating all of their child poses allows for a large fraction of the complete set of poses to be eliminated without the time-consuming energy evaluation.

The 100 selected poses are then further refined with sidechain optimization using SCREAM (S15). Any sidechain that was alanized prior to docking is now restored and optimized ("de-alanized") by SCREAM. Simultaneously, any polar or charged sidechain in the binding site is also optimized by SCREAM, resulting in 100 unique sets of sidechain conformations each adapted to a specific ligand pose. Each complex is then energy optimized for 10 steps of conjugate gradient minimization. The minimized complexes are then scored using the "snap" binding energy, which is the total energy of the protein and the total energy of the ligand subtracted from the total energy of the complex, all calculated using DREIDING and MPSim. We then eliminated half of these complexes based on these energies. The remaining half was optimized with an additional 50 steps of conjugate gradient minimization. These fully-minimized complexes were rescored again, and the top one or two poses identified for analysis.

Closest-Neighbor Seeded Ligand Clustering

The Closest-Neighbor Seeded (CNS) ligand clustering algorithm uses a RMSD-based metric to cluster ligands into families and to assign family heads. First, all pairwise ligand RMSDs were calculated (ignoring hydrogen atoms). These pairwise RMSDs were placed in a list ordered from smallest RMSD to largest. The pair of ligands with the smallest RMSD constitutes the seed for the first family/cluster. Proceeding down the list of pairs i and j, the following operations were carried out:

1. If pose *i* and pose *j* do not belong to a pre-existing family, then a new family is seeded

2. If pose *i* belongs to family *A* and pose *j* does not belong to a family (or *vice versa*): If the RMSD of pose *j* to all members of family *A* is less than the diversity RMSD, then pose *j* is added to family *A*

3. If pose *i* belongs to family *A* and pose *j* belongs to family *B*: If the RMSD of pose *i* to all members of family *B* is less than the diversity RMSD, and if the RMSD of pose *j* to all members of family *A* is less than the diversity RMSD, then the two families are merged into a single family

The pose with the lowest RMSD to the rest of the members is designated as the family head. If a family only has two members then the family head is chosen randomly.

Forcefield

All forcefield calculations during docking – with the exception of sidechain optimizations – were performed using the DREIDING (S2) forcefield and the MPSim (S14) molecular dynamics code. DREIDING uses a three body hydrogen bond term that allows a more precise analysis of the energetics. It also eliminates the need of SHAKE constraints that must be used with the 2-body hydrogen bonds used in most force fields

Sidechain Optimization

Sidechain optimization was performed using the SCREAM program (using the DREIDING forcefield.

Sphere Generation

Spheres were generated using a modified *sphgen* program (S13). Specifically, two sets of spheres were generated for each protein:

The "normal" set:

- Use a 1.4 Å probe radius in the *dms* molecular surface program (44)

- Use dotlim=–0.9 in *sphgen*

- Use 1.4 Å minimum and 10 Å maximum sphere radii in *sphgen*

The "restriction" set:

- Use 2.8 Å probe radius in *dms*

- Use dotlim=–0.9 ' in *sphgen*

- Use 2.8 Å minimum and 10 Å maximum sphere radii in *sphgen*

The final set of spheres is taken from the "normal" set with the criteria that a sphere must be within 2.8 Å of a sphere from the "restriction" set.

The final set of spheres was partitioned into overlapping boxes having 20 Å sides and allowing 5 Å overlap.

As mentioned above, we assign electrostatic potential values to the spheres. The electrostatic potential for the protein is generated using APBS (S16-S18) and mapped onto the generated spheres. The electrostatic potential for a given sphere is taken from the value from the nearest APBS grid point.

Sphere Clustering

In order to reduce the number of spheres in each region to a computationally-manageable number, the spheres are clustered using the CNS algorithm, with each sphere treated as a single-atom ligand. The clustering diversity is set at 0.25 and increased until the total

number of families is less than 150, or until the diversity is 3.00. For sphere families with 3 or more spheres, the family head is kept to represent the family. For sphere families of 2 spheres, the coordinates are averaged.

Ligand Preparation

All crystal structure ligands were prepared by identifying the appropriate DREIDING atom types and assigning Mulliken charges from Density Functional Theory (DFT) calculations using the B3LYP level of theory and the 6-311G** basis set in Jaguar (S19, S27).

Heparin and CS ligands for the predicted systems (RPTP**s**, NgR, EphB2, and EphB3) were generated from available 18-mer heparin NMR structures (S20) and a 6-mer CS-A (S21) crystal structure as mentioned above. The heparin and CS-A structures were truncated or extended as needed for docking. Generating CS-D and CS-E required modifying the sulfation pattern of an extended 12-mer CS-A structure.

The sulfation pattern was modified using the Maestro software, Mulliken charges were calculated, and the MacroModel (S22) Conformational Search tool was used to sample the sidechain torsions (the sugar backbone was kept fixed). The resulting conformations were minimized using DREIDING and MPSim with Surface Generalized Born (SGB) solvation. The lowest-energy conformation was then selected for MD.

The AMBER (S23) package was used to place the 12-mer in a water box with a number of sodium ions added to neutralize the ligand charge. Dynamics was performed using NAMD (S24) in four steps as described in the next section. Briefly, first, the water box was minimized with the ligand kept fixed. Second 0.5 ns of MD were performed on the water box. Third, the entire system was minimized. Finally, 5 ns of MD were performed on the

entire system. The final ligand conformation for docking was the conformation closest to the average structure from the 5 ns MD. The 12-mer was truncated for docking by removing the terminal sugars.

Molecular Dynamics (MD)

The MD simulations were carried out using NAMD (S24), a parallel MD code designed for computationally demanding biomolecular systems. The CHARMM (S1) force field was used for the protein and ligands. The TIP3P (S25) force field was used for water. NAMD employs periodic boundary conditions to remove surface effects. The full electrostatic interactions within this periodic system is calculated using the particle-mesh Ewald summation method (S26). The long-range electrostatic and van der Waals interactions were cut off at 12 Å (with spline smoothing).

The calculations were performed under isothermal-isobaric conditions (NPT) at 310 K and 1 atm. The temperature was controlled using Langevin dynamics (with a coupling coefficient of 5 ps^{-1}) and the pressure is maintained using a Langevin-Hoover barostat. A time step of 1 fs was used throughout this study.

Simulations. The MD is carried out in 4 steps:

a) The water atoms and counter-ions were conjugate gradient minimized for 5000 steps while keeping the protein and ligand atoms fixed. This allows for the water and counter ions to remove any bad contacts with each other and the protein or the ligand, prior to MD.

b) Then the water and counter-ion atoms were equilibrated under NPT conditions (310 K and 1 atm) for 0.5 ns, while keeping the protein and ligand fixed. This allows the lipids

and waters to equilibrate in the presence of the protein and to fill any gaps around the

protein created due to system setup.

c) Next, the full system (protein-ligand-water) was minimized for 5000 steps, allowing the

protein and ligand to adjust to the equilibrated water and counter ions.

d) Finally, the full system is equilibrated for at least 5 ns under NPT conditions, of which

only the last 5 ns is used for dynamical analysis. Snapshots are saved every 1 ps.

Supplemental References

S1. A D MacKerell, J., Bashford, D., Bellott, M., R L Dunbrack, J., Evanseck, J. D., Field, M. J., et al. (1998). All-Atom Empirical Potential for Molecular Modeling and Dynamics Studies of Proteins. *The Journal of Physical Chemistry B*, *102*(18), 3586–3616. http://doi.org/10.1021/jp973084f

S2. Mayo, S. L., Olafson, B. D., & Goddard, W. A. (2002). DREIDING: a generic force field for molecular simulations. *The Journal of Physical Chemistry*, *94*(26), 8897–8909. http://doi.org/10.1021/j100389a010

S3. Kim, D. E., Chivian, D., & Baker, D. (2004). Protein structure prediction and analysis using the Robetta server. *Nucleic Acids Research*, *32*(suppl 2), W526–W531. http://doi.org/10.1093/nar/gkh468

S4. Scott, C. E., Ahn, K. H., Graf, S. T., William A Goddard, I., Kendall, D. A., & Abrol, R. (2016). Computational Prediction and Biochemical Analyses of New Inverse Agonists for the CB1 Receptor. *Journal of Chemical Information and Modeling*, *56*(1), 201–212. http://doi.org/10.1021/acs.jcim.5b00581

S5. Li, Q., Kim, S.-K., Goddard, W. A., III, Chen, G., & Tan, H. (2015). Predicted Structures for Kappa Opioid G-Protein Coupled Receptor Bound to Selective Agonists. *Journal of Chemical Information and Modeling*, *55*(3), 614–627. http://doi.org/10.1021/ci500523z

S6. Abrol, R., Trzaskowski, B., Goddard, W. A., III, Nesterov, A., Olave, I., & Irons, C. (2014). Ligand- and mutation-induced conformational selection in the CCR5 chemokine G protein-coupled receptor. *Proceedings of the National Academy of Sciences*, *111*(36), 13040–13045. http://doi.org/10.1073/pnas.1413216111

S7. Bray, J. K., Abrol, R., Goddard, W. A., III, Trzaskowski, B., & Scott, C. E. (2014). SuperBiHelix method for predicting the pleiotropic ensemble of G-protein–coupled receptor conformations. *Proceedings of the National Academy of Sciences*, *111*(1), E72–E78. http://doi.org/10.1073/pnas.1321233111

S8. Kim, S.-K., & Goddard, W. A. (2014). Predicted 3D structures of olfactory receptors with details of odorant binding to OR1G1. *Journal of Computer-Aided Molecular Design*, *28*(12), 1175–1190. http://doi.org/10.1007/s10822-014-9793-4

S9. Kim, S.-K., Goddard, W. A., Yi, K. Y., Lee, B. H., Lim, C. J., & Trzaskowski, B. (2014). Predicted Ligands for the Human Urotensin-II G Protein-Coupled Receptor with Some Experimental Validation. *ChemMedChem*, *9*(8), 1732–1743. http://doi.org/10.1002/cmdc.201402087

S10. Tan, J., Abrol, R., Trzaskowski, B., & William A Goddard, I. (2012). 3D Structure Prediction of TAS2R38 Bitter Receptors Bound to Agonists Phenylthiocarbamide (PTC) and 6-n-Propylthiouracil (PROP). *Journal of Chemical Information and Modeling*, *52*(7), 1875–1885. http://doi.org/10.1021/ci300133a

S11. Kim, S.-K., Fristrup, P., Abrol, R., & William A Goddard, I. (2011a). Structure-Based Prediction of Subtype Selectivity of Histamine H3 Receptor Selective Antagonists in Clinical Trials. *Journal of Chemical Information and Modeling*, *51*(12), 3262–3274. http://doi.org/10.1021/ci200435b

S12. Kim, S.-K., Riley, L., Abrol, R., Jacobson, K. A., & Goddard, W. A. (2011b). Predicted structures of agonist and antagonist bound complexes of adenosine A3 receptor. *Proteins: Structure, Function, and Bioinformatics*, *79*(6), 1878–1897. http://doi.org/10.1002/prot.23012

S13. Allen, W. J., Balius, T. E., Mukherjee, S., Brozell, S. R., Moustakas, D. T., Lang, P. T., et al. (2015). DOCK 6: Impact of new features and current docking performance. *Journal of Computational Chemistry*, *36*(15), 1132–1156. http://doi.org/10.1002/jcc.23905

S14. Lim, K. T., Brunett, S., Iotov, M., & McClurg, R. B. (1997). Molecular dynamics for very large systems on massively parallel computers: the MPSim program. *Journal of Computational Chemistry*, *18*(4), 501-521

S15. Kam, V. W. T., & William A Goddard, I. (2008). Flat-Bottom Strategy for Improved Accuracy in Protein Side-Chain Placements. *Journal of Chemical Theory and Computation*, *4*(12), 2160–2169. http://doi.org/10.1021/ct800196k

S16. Baker, N. A., Sept, D., Joseph, S., Holst, M. J., & McCammon, J. A. (2001). Electrostatics of nanosystems: Application to microtubules and the ribosome. *Proceedings of the National Academy of Sciences*, *98*(18), 10037–10041. http://doi.org/10.1073/pnas.181342398

S17. Dolinsky, T. J., Czodrowski, P., Li, H., Nielsen, J. E., Jensen, J. H., Klebe, G., & Baker, N. A. (2007). PDB2PQR: expanding and upgrading automated preparation of biomolecular structures for molecular simulations. *Nucleic Acids Research*, *35*(suppl 2), W522–W525. http://doi.org/10.1093/nar/gkm276

S18. Dolinsky, T. J., Nielsen, J. E., McCammon, J. A., & Baker, N. A. (2004). PDB2PQR: an automated pipeline for the setup of Poisson–Boltzmann electrostatics calculations. *Nucleic Acids Research*, *32*(suppl 2), W665–W667. http://doi.org/10.1093/nar/gkh381

S19. Jaguar, version 8.9, Schrödinger, LLC, New York, NY, 2015.

S20. Khan, S., Gor, J., Mulloy, B., & Perkins, S. J. (2010). Semi-Rigid Solution Structures of Heparin by Constrained X-ray Scattering Modelling: New Insight into Heparin–Protein Complexes. *Journal of Molecular Biology*, *395*(3), 504–521. http://doi.org/10.1016/j.jmb.2009.10.064

S21. Winter, W. T., Arnott, S., Isaac, D. H., & Atkins, E. D. T. (1978). Chondroitin 4-sulfate: The structure of a sulfated glycosaminoglycan. *Journal of Molecular Biology*, *125*(1), 1–19. http://doi.org/10.1016/0022-2836(78)90251-6

S22. MacroModel, version 10.9, Schrödinger, LLC, New York, NY, 2015.

S23. D.A. Case, R.M. Betz, W. Botello-Smith, D.S. Cerutti, T.E. Cheatham, III, T.A. Darden, R.E. Duke, T.J. Giese, H. Gohlke, A.W. Goetz, N. Homeyer, S. Izadi, P. Janowski, J. Kaus, A. Kovalenko, T.S. Lee, S. LeGrand, P. Li, C. Lin, T. Luchko, R. Luo, B. Madej, D. Mermelstein, K.M. Merz, G. Monard, H. Nguyen, H.T. Nguyen, I. Omelyan, A. Onufriev, D.R. Roe, A. Roitberg, C. Sagui, C.L. Simmerling, J. Swails, R.C. Walker, J. Wang, R.M. Wolf, X. Wu, L. Xiao, D.M. York and P.A. Kollman (2016), AMBER 2016, University of California, San Francisco.

S24. Phillips, J. C., Braun, R., Wang, W., Gumbart, J., Tajkhorshid, E., Villa, E., et al. (2005). Scalable molecular dynamics with NAMD. *Journal of Computational Chemistry*, *26*(16), 1781–1802. http://doi.org/10.1002/jcc.20289.

S25. Jorgensen, W. L., Chandrasekhar, J., Madura, J. D., Impey, R. W., & Klein, M. L. (1983). Comparison of simple potential functions for simulating liquid water. *The Journal of Chemical Physics*, *79*(2), 926–935. http://doi.org/10.1063/1.445869

S26. Darden, T., York, D., & Pedersen, L. (1993). Particle mesh Ewald: An N·log(N) method for Ewald sums in large systems. *The Journal of Chemical Physics*, *98*(12), 10089–10092. http://doi.org/10.1063/1.464397

S27. Bochevarov, A. D., Harder, E., Hughes, T. F., Greenwood, J. R., Braden, D. A., Philipp, D. M., et al. (2013). Jaguar: A high-performance quantum chemistry software program with strengths in life and materials sciences. *International Journal of Quantum Chemistry*, *113*(18), 2110–2142. http://doi.org/10.1002/qua.24481
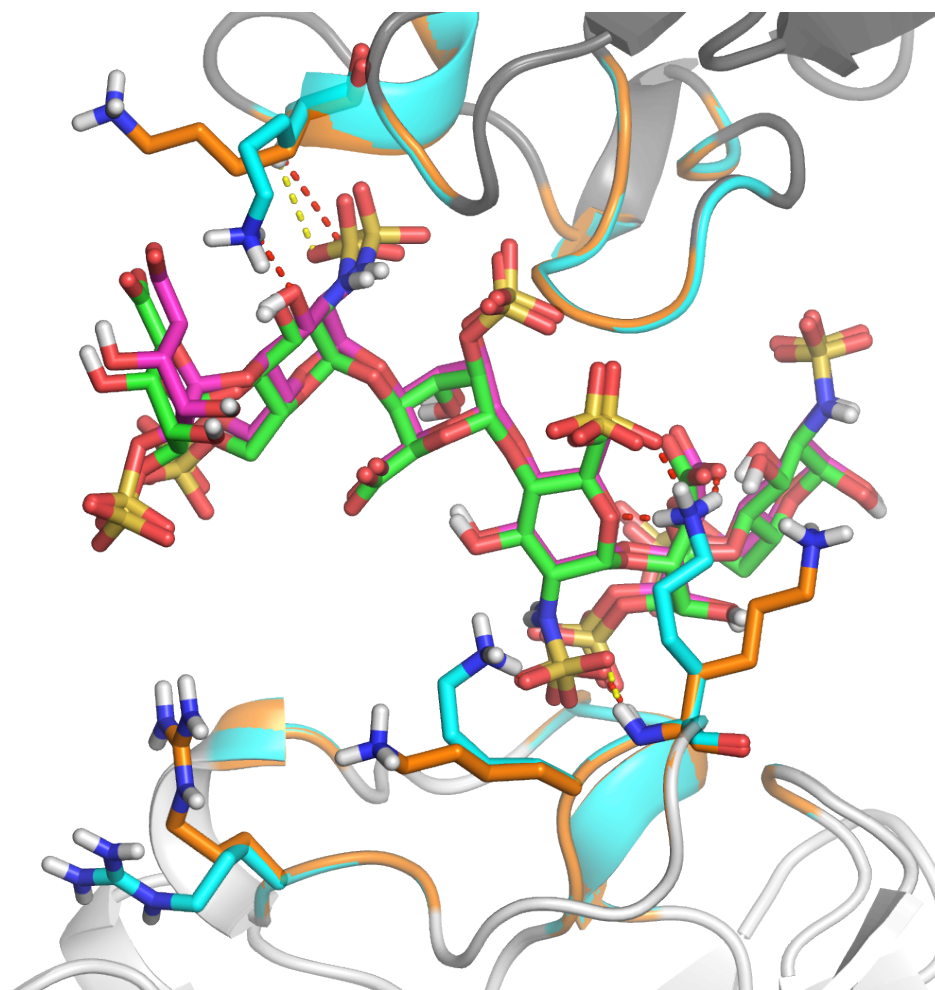
Supplemental Figures & Tables

Figure S3-5 – Structure of FGF1 [PDB: 2AXM, resolution 3.00 Å] with predicted and crystal heparin hexamer ligands (magenta: predicted, green: crystal). Residues in the binding site with significant deviations from the crystal are labeled (cyan: predicted, orange: crystal). Ligand RMSD is 0.70 Å.
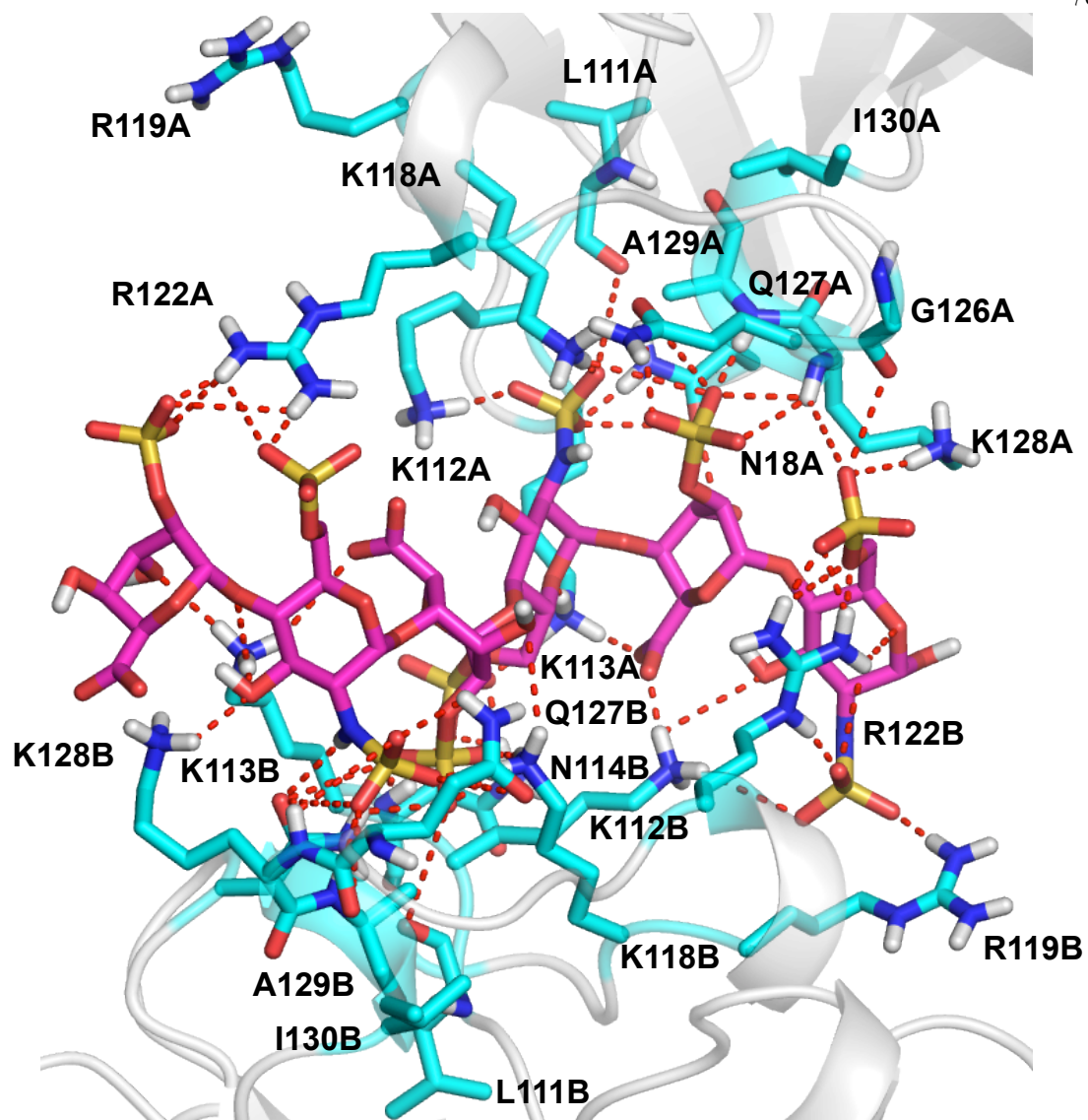
Figure S3-6– Structure of FGF1 [PDB: 2AXM, res. 3.00 Å] with predicted heparin hexamer ligand (magenta) and 5 Å binding site shown (cyan). Dashed lines indicate hydrogen bonding and salt bridges between ligand and protein. The predicted ligand has excellent agreement with the crystal ligand, RMSD: 0.70 Å.

Figure S3-7 – Structure of FGF2 [PDB: 1BFB, res. 1.90 Å] with predicted heparin tetramer ligand (magenta) and 5 Å binding site shown (cyan). Dashed lines indicate hydrogen bonding and salt bridges between ligand and protein. The predicted ligand has excellent agreement with the crystal ligand, RMSD: 0.70 Å.

Figure S3-8 – Structure of FGF2-FGFR1 [PDB: 1FQ9, res. 3.00 Å] chain A with predicted heparin hexamer ligand (magenta) and 5 Å binding site shown (cyan). Dashed lines indicate hydrogen bonding and salt bridges between ligand and protein. The predicted ligand has excellent agreement with the crystal ligand, RMSD: 1.51/0.75 Å.

Figure S3-9 – Structure of FGF2-FGFR1 [PDB: 1FQ9, res. 3.00 Å] chain B with predicted heparin hexamer ligand (magenta) and 5 Å binding site shown (cyan). Dashed lines indicate hydrogen bonding and salt bridges between ligand and protein. The predicted ligand has excellent agreement with the crystal ligand, RMSD: 1.51/0.75 Å.
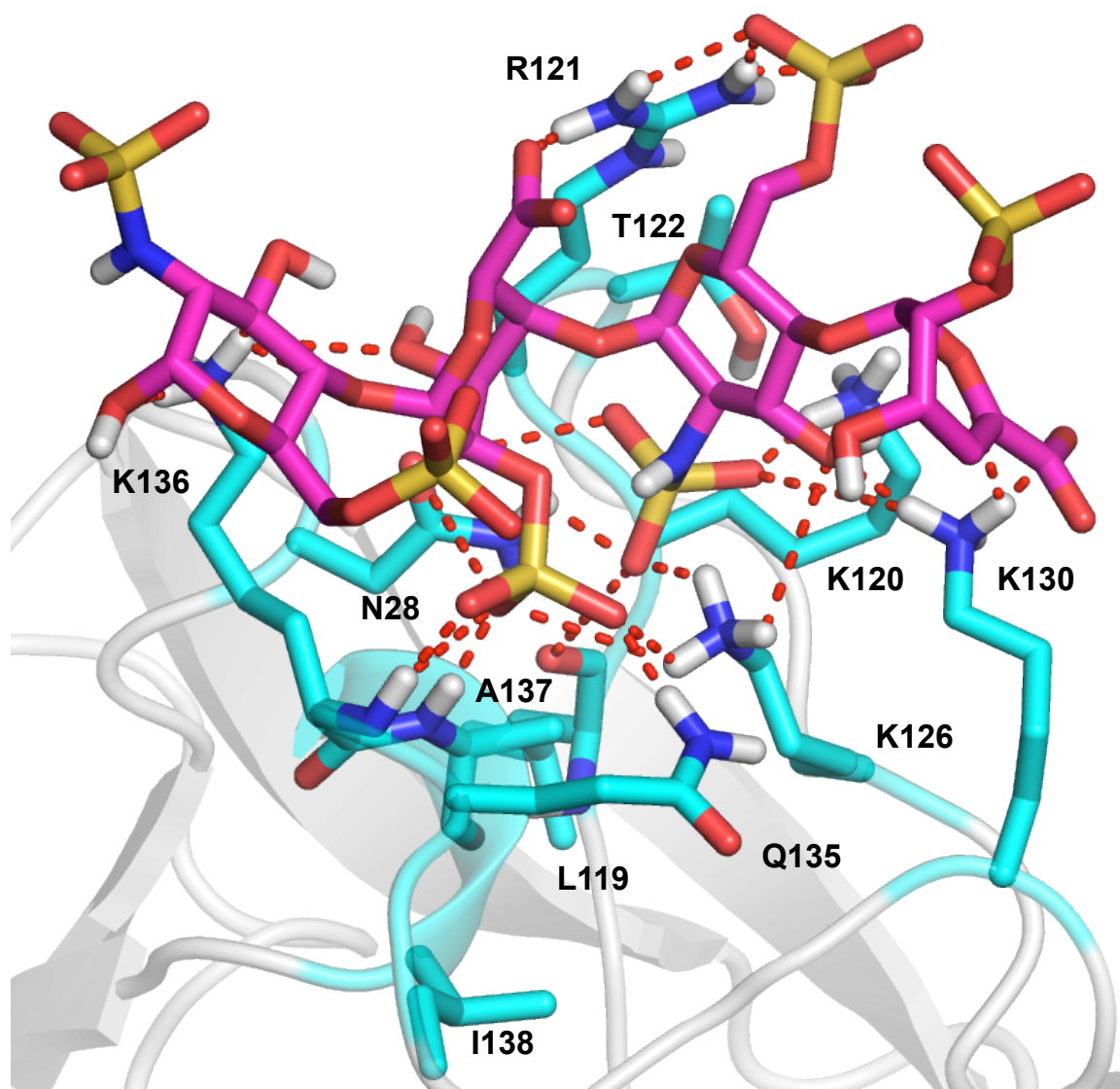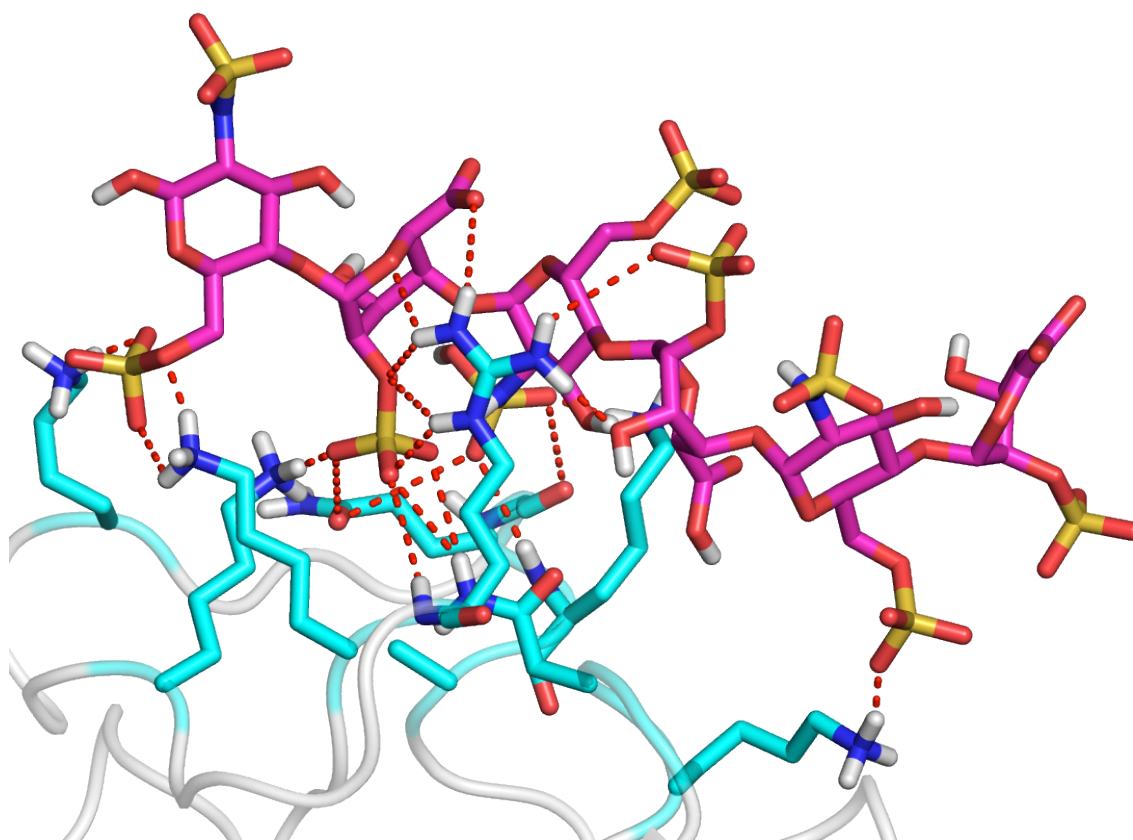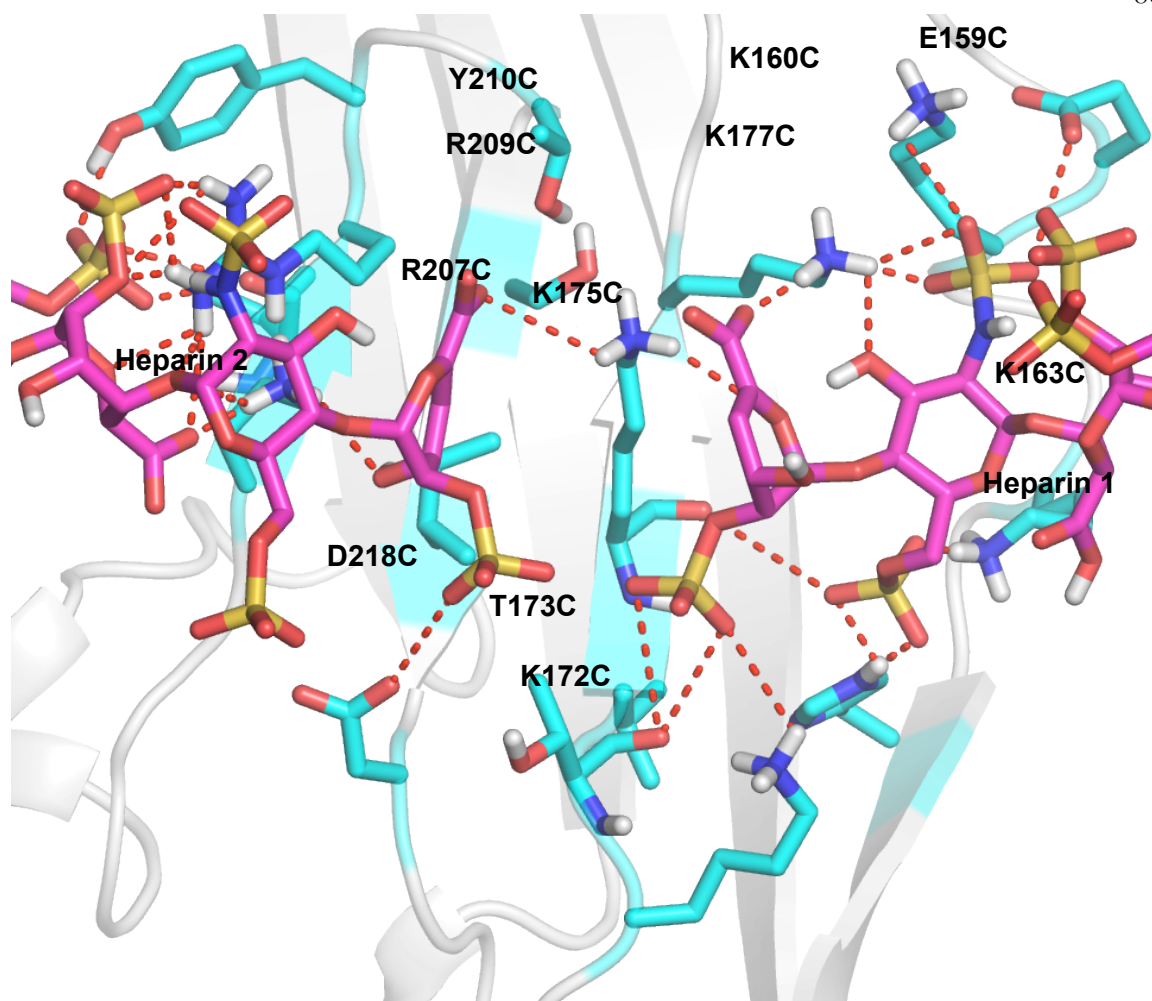
Figure S3-10 – Structure of FGF2-FGFR1 [PDB: 1FQ9, res. 3.00 Å] chain C with predicted heparin hexamer and octamer ligands (magenta) and 5 Å binding site shown (cyan). Dashed lines indicate hydrogen bonding and salt bridges between ligand and protein. The predicted ligand has excellent agreement with the crystal ligand, RMSD: 1.51/0.75 Å.
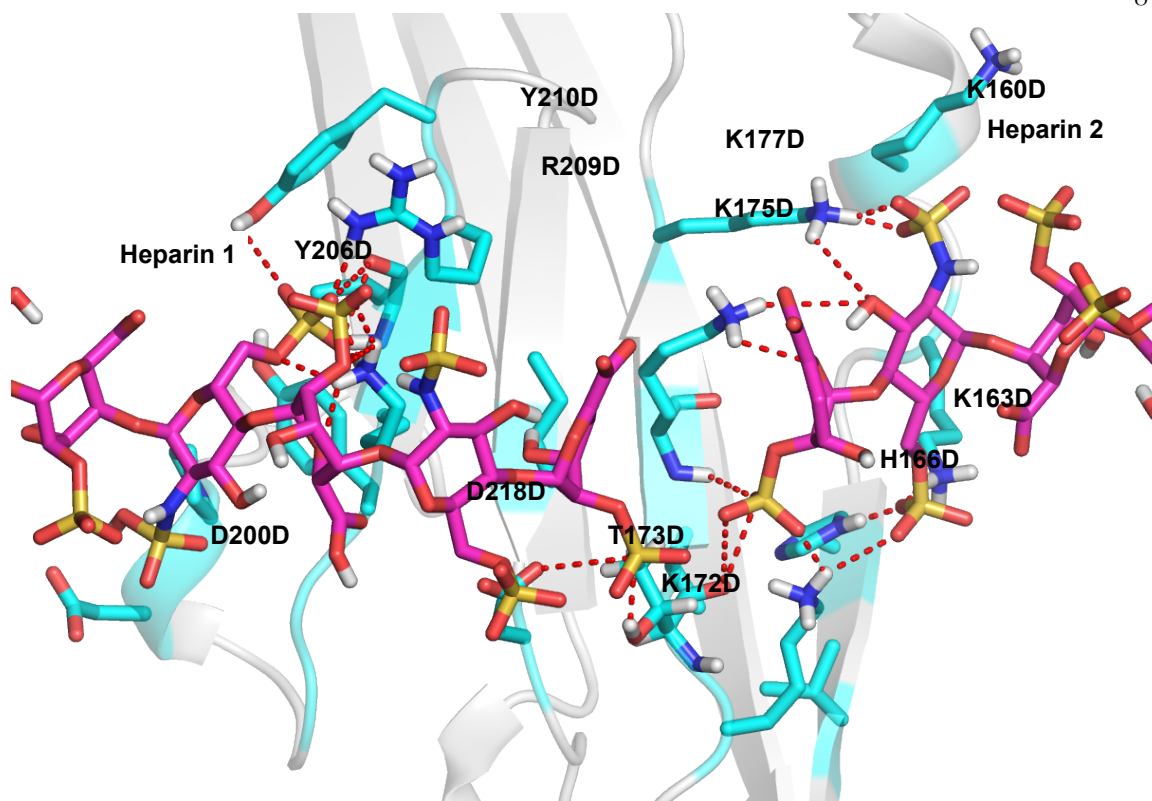
Figure S3-11 – Structure of FGF2-FGFR1 [PDB: 1FQ9, res. 3.00 Å] chain C with predicted heparin hexamer and octamer ligands (magenta) and 5 Å binding site shown (cyan). Dashed lines indicate hydrogen bonding and salt bridges between ligand and protein. The predicted ligand has excellent agreement with the crystal ligand, RMSD: 1.51/0.75 Å.
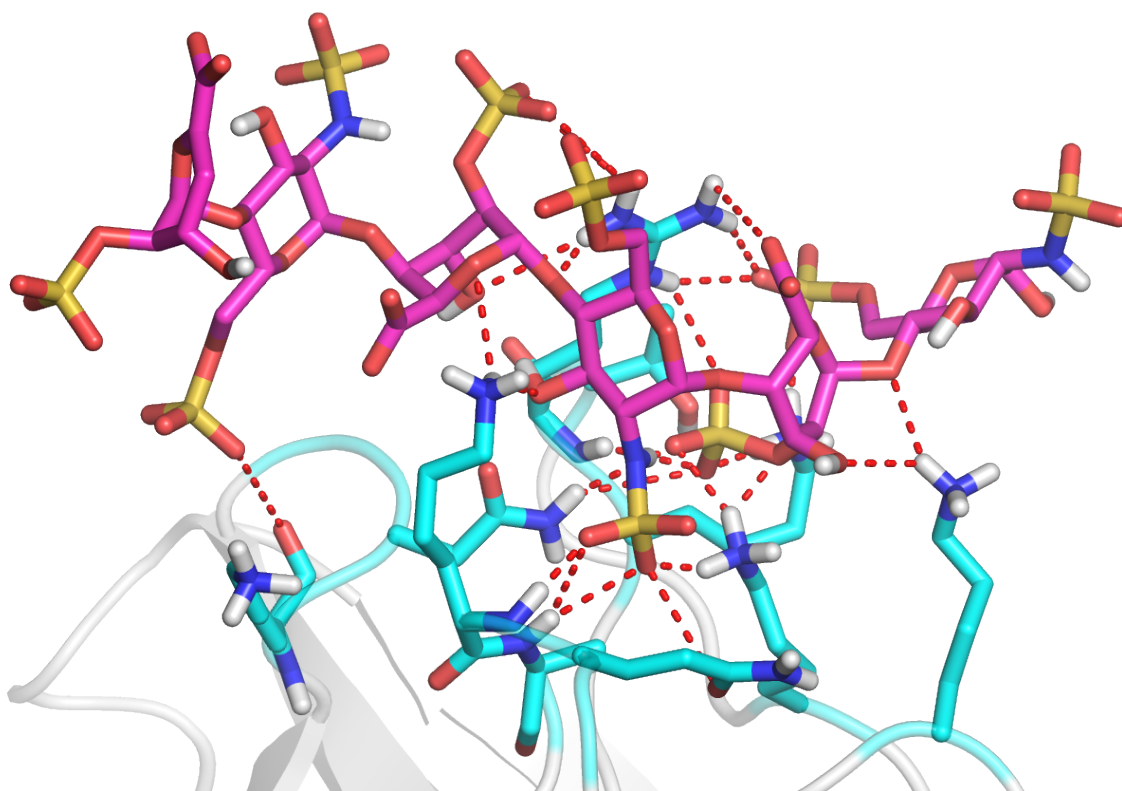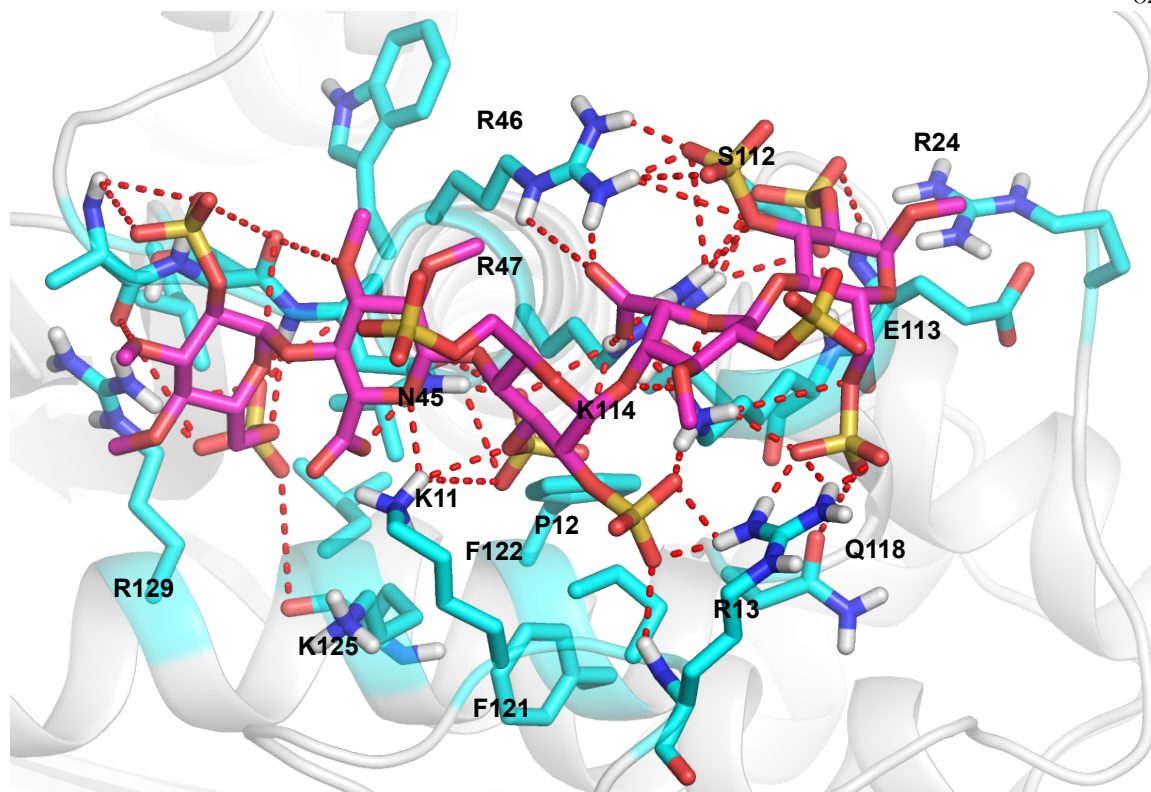
Figure S3-12 – Structure of α-Antithrombin-III [PDB: 1E03, res. 2.90 Å] with predicted heparin analog pentamer ligand (magenta) and 5 Å binding site shown (cyan). Dashed lines indicate hydrogen bonding and salt bridges between ligand and protein. The predicted ligand has excellent agreement with the crystal ligand, RMSD: 0.60 Å.

Figure S3-13 – Plots of nonbond energies for residues in the (A) FGF1, (B) FGF2, (C) FGF2-FGFR1 Chain A complex, (D) FGF2-FGFR1 Chain B complex, and (E) α-Antithrombin-III binding sites in complex with a heparin ligand in the crystal versus docked structure. Residues with significant deviations from the trend are labeled.

Table S3-5 – Per-residue energetic contributions in the FGF1/heparin predicted (left) and crystal (right) structures. [PDB: 2AXM, res. 3.00 Å, RMSD: 0.70 Å].

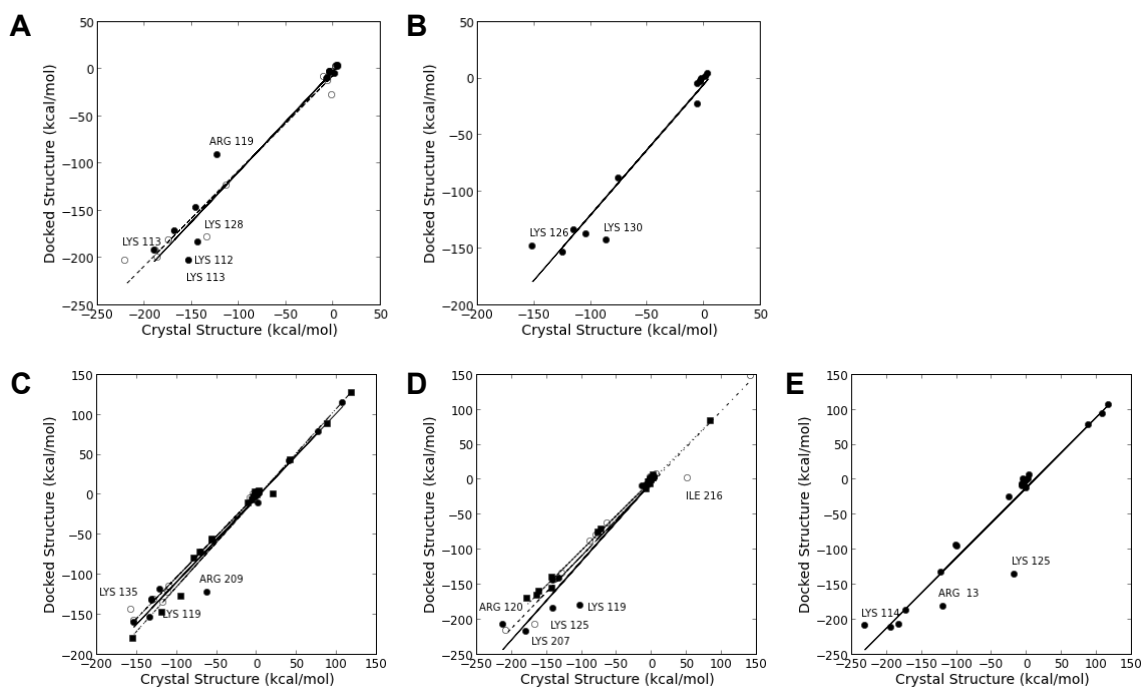|	Residue	Docked				Crystal				
		VdW	Coulomb	H Bond	NonBond	VdW	Coulomb	H Bond	NonBond	$\Delta_{NonBond}$
	LYS 113	17.56	-204.76	-15.75	-202.95	2.77	1.19	-2.00	1.96	-204.91
	LYS 118	3.22	-189.23	-5.96	-191.97	-0.56	4.09	0.00	3.54	-195.51
	LYS 112	3.29	-183.50	-3.81	-184.01	-0.33	-143.67	0.00	-144.00	-40.01
	ARG 122	7.16	-169.14	-9.33	-171.31	3.14	-153.18	-3.12	-153.17	-18.14
	LYS 128	3.06	-148.57	-1.85	-147.37	-0.41	4.77	0.00	4.37	-151.74
Chain A	ARG 119	-0.11	-91.00	0.00	-91.11	-0.06	-3.21	0.00	-3.27	-87.84
	GLN 127	-2.00	-8.03	0.00	-10.03	-1.99	-186.44	-1.59	-190.03	180.00
	ALA 129	5.47	-10.00	-4.60	-9.14	-0.38	-122.47	0.00	-122.86	113.72
	ASN 18	2.01	-1.44	-5.71	-5.13	-1.52	-165.54	-1.67	-168.72	163.59
	ILE 130	-0.32	-3.07	0.00	-3.39	-0.88	5.58	0.00	4.70	-8.08
	GLY 115	-0.04	-3.22	0.00	-3.27	-0.13	-6.95	0.00	-7.08	3.81
	GLY 126	-0.87	3.54	0.00	2.66	-4.08	-140.24	-1.57	-145.89	148.55
	LEU 111	-0.48	3.51	0.00	3.03	3.28	-8.41	-1.05	-6.18	9.21
	ASN 114	-0.23	3.33	0.00	3.10	-0.30	-2.97	0.00	-3.28	6.38
	LYS 113	4.89	-197.61	-9.67	-202.39	1.11	-215.76	-5.84	-220.49	18.10
	LYS 112	4.24	-198.73	-5.46	-199.96	2.69	-190.94	-0.44	-188.69	-11.26
	LYS 118	11.00	-197.81	-5.73	-192.53	-4.61	-181.97	0.00	-186.58	-5.96
	ARG 122	4.88	-176.18	-10.38	-181.68	2.69	-175.17	-1.89	-174.37	-7.31
	LYS 128	10.38	-181.92	-6.98	-178.52	2.06	-135.42	0.00	-133.36	-45.16
Chain B	ARG 119	7.42	-125.16	-5.83	-123.58	-2.11	-111.44	0.00	-113.55	-10.03
	ASN 114	5.11	-22.15	-10.47	-27.51	-0.34	-7.68	-1.92	-9.94	-17.57
	GLN 127	2.94	-13.43	-1.56	-12.05	-0.60	-5.77	0.00	-6.37	-5.68
	ALA 129	6.73	-10.22	-4.49	-7.99	-0.14	-3.90	0.00	-4.04	-3.94
	GLY 115	-0.14	-4.03	0.00	-4.17	-0.27	-2.84	0.00	-3.11	-1.07
	ILE 130	-0.37	-3.13	0.00	-3.50	-1.63	2.88	-3.24	-1.99	-1.50
	ASN 18	0.24	2.05	-5.05	-2.76	-2.38	1.24	-0.18	-1.32	-1.44
	GLY 126	-0.24	2.42	0.00	2.18	-0.56	2.92	0.00	2.36	-0.17
	LEU 111	-0.72	2.97	0.00	2.25	-0.25	2.86	0.00	2.61	-0.36

Table S3-6 – Per-residue energetic contributions in the FGF2/heparin predicted (left) and crystal (right) structures. [PDB: 1BFB, res. 1.90 Å, RMSD: 0.70 Å].

	Residue	Docked				Crystal				
		VdW	Coulomb	H Bond	NonBond	VdW	Coulomb	H Bond	NonBond	$\Delta_{NonBond}$
	ARG 121	17.30	-158.68	-12.19	-153.56	-0.27	-150.23	-0.96	-151.45	-2.11
	LYS 126	9.10	-156.65	-0.36	-147.92	-3.44	-119.39	-2.31	-125.14	-22.78
	LYS 130	10.15	-144.73	-8.56	-143.15	-5.00	-107.74	-1.75	-114.49	-28.65
	LYS 120	8.16	-140.09	-5.58	-137.52	-2.88	-101.57	0.00	-104.45	-33.07
	LYS 136	6.73	-135.14	-5.78	-134.19	-0.75	-85.16	0.00	-85.91	-48.28
Chain A	LYS 27	-0.42	-87.54	0.00	-87.96	-0.28	-75.32	0.00	-75.60	-12.37
	GLN 135	2.17	-18.79	-6.09	-22.72	-2.77	-2.99	0.00	-5.76	-16.96
	ALA 137	7.94	-9.51	-3.59	-5.16	5.61	-8.31	-2.66	-5.37	0.21
	ILE 138	-0.28	-2.34	0.00	-2.62	-2.44	1.25	-1.53	-2.72	0.10
	ASN 28	3.07	-1.79	-3.76	-2.47	-0.28	-2.29	0.00	-2.57	0.10
	THR 122	-0.40	0.02	0.00	-0.37	-0.31	-1.32	0.00	-1.63	1.26
	GLY 134	-0.37	2.18	0.00	1.81	-0.43	2.34	0.00	1.92	-0.11
	LEU 119	-0.62	4.44	0.00	3.82	-0.45	4.03	0.00	3.57	0.25

Table S3-7 – Per-residue energetic contributions in the FGF2-FGFR1/heparin predicted (left) and crystal (right) structures for chains A and B. [PDB: 1FQ9, res. 3.00 Å, RMSD: 1.51/0.75 Å].

	Residue	Docked				Crystal				$\Delta_{NonBond}$
		VdW	Coulomb	H Bond	NonBond	VdW	Coulomb	H Bond	NonBond	
	ARG 120	-2.28	-149.49	-5.26	-157.04	1.52	-152.06	-7.27	-157.81	0.77
	LYS 135	1.54	-139.58	-5.91	-143.95	4.60	-153.99	-3.79	-153.18	9.24
	LYS 119	0.67	-131.00	-4.78	-135.12	3.14	-130.93	-0.25	-128.04	-7.08
	LYS 125	5.84	-131.09	-5.87	-131.11	0.62	-116.95	-0.65	-116.98	-14.13
	LYS 26	4.39	-120.65	-5.68	-121.94	-1.02	-109.45	0.00	-110.47	-11.47
	LYS 129	4.99	-114.65	-5.58	-115.25	-1.24	-107.92	-0.68	-109.84	-5.41
Chain A	ALA 136	-0.53	-3.71	0.00	-4.24	2.86	-6.00	-4.60	-7.74	3.51
	GLY 28	-0.37	-2.08	0.00	-2.45	-2.02	1.97	-3.62	-3.67	1.22
	ILE 137	-0.12	-1.95	0.00	-2.07	-0.66	-1.95	0.00	-2.61	0.53
	GLN 134	-1.91	0.68	0.00	-1.23	-0.29	-2.08	0.00	-2.36	1.14
	ASN 27	-1.89	2.20	0.00	0.31	-0.48	-1.59	0.00	-2.08	2.39
	THR 121	-0.20	0.54	0.00	0.34	-0.17	-1.53	0.00	-1.70	2.04
	TYR 24	-0.14	1.63	0.00	1.49	4.63	-4.77	0.00	-0.14	1.63
	LEU 118	-0.15	2.35	0.00	2.20	-0.31	2.16	0.00	1.85	0.35
	GLY 133	-0.32	2.55	0.00	2.23	-0.50	2.69	0.00	2.19	0.04
	LEU 126	-0.14	2.56	0.00	2.42	-0.28	2.62	0.00	2.34	0.08
	LYS 135	1.19	-212.03	-6.46	-217.30	-8.49	-203.03	-1.48	-212.99	-4.31
	ARG 120	-6.58	-199.88	-1.36	-207.81	31.40	-208.27	-3.53	-180.39	-27.41
	LYS 125	5.60	-182.56	-6.84	-183.80	38.12	-175.56	-3.61	-141.05	-42.75
	LYS 119	12.36	-181.40	-10.45	-179.49	-2.14	-138.68	0.00	-140.82	-38.67
	LYS 129	-1.92	-141.31	-0.25	-143.48	-1.59	-130.86	0.00	-132.44	-11.04
Chain B	LYS 26	-2.18	-138.89	0.00	-141.07	37.15	-138.94	0.00	-101.78	-39.29
	GLN 134	-2.27	-6.73	0.00	-9.00	9.71	-20.50	-3.13	-13.92	4.92
	ALA 136	-1.24	-7.10	0.00	-8.34	-1.58	-6.76	0.00	-8.33	-0.01
	GLY 28	-0.34	-3.40	0.00	-3.74	-0.40	-2.89	0.00	-3.29	-0.45
	THR 121	-1.70	2.18	0.00	0.48	-0.16	-1.81	0.00	-1.97	2.44
	ASN 27	-2.39	4.25	0.00	1.86	3.82	-3.11	-0.03	0.68	1.18
	TYR 24	-0.15	2.25	0.00	2.10	-2.71	5.94	-0.05	3.18	-1.08
	GLY 133	-0.21	3.30	0.00	3.09	-0.25	3.55	0.00	3.30	-0.22
	LEU 118	-0.33	3.65	0.00	3.32	-0.52	3.96	0.00	3.44	-0.12

Table S3-8 – Per-residue energetic contributions in the FGF2-FGFR1/heparin-A predicted (left) and crystal (right) structures for chain C. [PDB: 1FQ9, res. 3.00 Å, RMSD: 1.51/0.75 Å].

	Residue		Docked				Crystal			
		VdW	Coulomb	H Bond	NonBond	VdW	Coulomb	H Bond	NonBond	Δ_{NonBond}
	LYS 177	7.03	-159.17	-8.16	-160.30	5.72	-158.41	-1.26	-153.95	-6.35
	LYS 175	0.73	-149.86	-4.69	-153.82	2.31	-130.03	-5.88	-133.60	-20.22
	LYS 163	6.37	-132.42	-6.11	-132.16	1.23	-132.09	-0.39	-131.25	-0.91
	LYS 160	0.37	-131.48	0.00	-131.12	-1.30	-129.72	-0.02	-131.03	-0.08
	ARG 209	-0.44	-117.34	-4.40	-122.18	-0.82	-120.14	0.00	-120.97	-1.21
	LYS 172	-0.78	-118.38	0.00	-119.16	-0.04	-70.04	0.00	-70.08	-49.08
	LYS 207	-0.04	-71.70	0.00	-71.75	-0.04	-61.48	0.00	-61.53	-10.22
	HSE 166	5.52	-12.11	-4.86	-11.44	-1.33	-3.41	0.00	-4.74	-6.70
	VAL 174	-0.99	-3.05	0.00	-4.04	-0.41	-2.90	0.00	-3.30	-0.74
Chain C	ILE 216	-0.52	-3.02	0.00	-3.54	-0.02	-1.90	0.00	-1.92	-1.62
	SER 219	-0.02	-1.90	0.00	-1.92	-0.02	-1.66	0.00	-1.68	-0.24
	TYR 206	-0.02	-1.58	0.00	-1.60	-0.01	-0.82	0.00	-0.83	-0.76
	VAL 208	-0.02	-0.86	0.00	-0.87	0.00	0.29	0.00	0.29	-1.16
	PRO 199	0.00	0.24	0.00	0.24	0.00	1.09	0.00	1.09	-0.85
	THR 173	-1.59	2.37	0.00	0.79	0.00	1.64	0.00	1.64	-0.85
	GLY 204	0.00	1.13	0.00	1.13	-1.28	3.00	0.00	1.72	-0.59
	GLY 205	0.00	1.63	0.00	1.63	-1.73	3.49	0.00	1.76	-0.13
	TYR 210	-0.02	2.19	0.00	2.18	-0.01	1.86	0.00	1.84	0.33
	ASP 200	0.00	41.39	0.00	41.39	0.00	41.11	0.00	41.10	0.28
	ASP 218	-0.09	78.09	0.00	78.01	-0.08	77.16	0.00	77.08	0.93
	GLU 159	-0.71	115.33	0.00	114.62	-0.45	107.49	0.00	107.04	7.59

Table S3-9 – Per-residue energetic contributions in the FGF2-FGFR1/heparin-A predicted (left) and crystal (right) structures for chain D. [PDB: 1FQ9, res. 3.00 Å, RMSD: 1.51/0.75 Å].

| | Residue | Docked | | | | Crystal | | | | |
		VdW	Coulomb	H Bond	NonBond	VdW	Coulomb	H Bond	NonBond	$\Delta_{NonBond}$
	LYS 207	7.45	-180.81	-6.56	-179.92	17.13	-171.90	-0.35	-155.12	-24.79
	ARG 209	3.65	-146.18	-5.18	-147.70	-0.83	-117.34	0.00	-118.16	-29.54
	LYS 175	5.98	-126.60	-6.24	-126.87	-0.40	-94.29	0.00	-94.69	-32.18
	LYS 172	-0.12	-79.28	0.00	-79.40	-0.12	-78.00	0.00	-78.11	-1.29
	LYS 177	-0.04	-72.16	0.00	-72.20	-0.03	-70.11	0.00	-70.14	-2.06
	LYS 160	-0.01	-56.66	0.00	-56.66	0.00	-55.42	0.00	-55.42	-1.25
	LYS 163	-0.01	-56.16	0.00	-56.16	-0.01	-55.17	0.00	-55.17	-0.99
	THR 173	3.72	-10.80	-3.54	-10.63	5.19	-10.69	-4.75	-10.26	-0.37
	TYR 210	-0.96	-5.72	0.00	-6.69	-0.25	-5.06	0.00	-5.30	-1.38
Chain D	PRO 199	-1.08	-2.70	0.00	-3.77	-0.45	-2.77	0.00	-3.23	-0.55
	HSE 166	-0.01	-2.21	0.00	-2.22	-0.01	-2.10	0.00	-2.11	-0.12
	GLY 205	-0.32	0.09	0.00	-0.23	-0.12	-1.83	0.00	-1.95	1.72
	ILE 216	0.51	-0.44	0.00	0.07	-0.22	0.36	0.00	0.14	-0.07
	TYR 206	-0.82	1.99	0.00	1.18	-0.69	3.14	0.00	2.45	-1.28
	SER 219	-0.10	2.54	0.00	2.44	-0.30	2.83	0.00	2.53	-0.08
	GLY 204	-0.30	2.82	0.00	2.52	-0.14	3.05	0.00	2.91	-0.39
	VAL 174	-0.15	3.01	0.00	2.86	-1.07	4.05	0.00	2.98	-0.12
	VAL 208	-1.09	5.42	-0.55	3.78	20.87	-0.03	0.00	20.85	-17.07
	GLU 159	0.00	43.02	0.00	43.02	0.00	42.22	0.00	42.22	0.80
	ASP 200	-0.29	88.12	0.00	87.83	-0.18	89.15	0.00	88.97	-1.14
	ASP 218	-2.17	129.70	0.00	127.53	-1.74	120.80	0.00	119.06	8.47

Table S3-10 – Per-residue energetic contributions in the FGF2-FGFR1/heparin-B predicted (left) and crystal (right) structures for chain C. [PDB: 1FQ9, res. 3.00 Å, RMSD: 1.51/0.75 Å].

| | Residue | Docked | | | | Crystal | | | | |
		VdW	Coulomb	H Bond	NonBond	VdW	Coulomb	H Bond	NonBond	$\Delta_{NonBond}$
	ARG 209	1.18	-211.75	-4.98	-215.55	-5.88	-198.45	-3.76	-208.09	-7.46
	LYS 207	12.57	-210.11	-9.85	-207.39	38.55	-204.68	-1.08	-167.22	-40.17
	LYS 175	7.82	-136.79	-5.80	-134.77	-0.95	-127.70	0.00	-128.65	-6.12
	LYS 177	-0.07	-88.11	0.00	-88.18	-0.06	-87.73	0.00	-87.79	-0.39
	LYS 172	-0.05	-79.78	0.00	-79.83	-0.04	-79.56	0.00	-79.60	-0.23
	LYS 160	-0.01	-76.48	0.00	-76.49	-0.01	-76.64	0.00	-76.65	0.16
	LYS 163	-0.01	-63.13	0.00	-63.14	-0.01	-63.12	0.00	-63.12	-0.02
Chain C	TYR 210	1.90	-7.94	-3.75	-9.79	-0.36	-6.01	0.00	-6.37	-3.42
	THR 173	-0.99	-7.60	0.00	-8.59	-0.78	-5.25	0.00	-6.03	-2.56
	VAL 168	-0.01	-1.12	0.00	-1.13	-0.01	-1.10	0.00	-1.11	-0.02
	SER 214	-0.31	0.98	0.00	0.68	-0.25	-1.54	0.00	-1.79	2.47
	HSE 166	-0.01	1.28	0.00	1.28	-0.01	1.35	0.00	1.34	-0.07
	ILE 216	2.12	-0.30	0.00	1.82	51.25	-0.18	0.00	51.07	-49.25
	VAL 174	-0.12	3.36	0.00	3.24	-0.10	3.33	0.00	3.24	0.01
	THR 212	-0.65	4.14	0.00	3.49	-0.55	-1.10	0.00	-1.65	5.14
	VAL 208	-1.18	8.37	0.00	7.19	-0.79	8.04	0.00	7.24	-0.05
	ASP 218	-0.99	148.97	0.00	147.98	-0.74	142.16	0.00	141.42	6.56

Table S3-11 – Per-residue energetic contributions in the FGF2-FGFR1/heparin-B predicted (left) and crystal (right) structures for chain D. [PDB: 1FQ9, res. 3.00 Å, RMSD: 1.51/0.75 Å].

	Residue	Docked				Crystal				$\Delta_{NonBond}$
		VdW	Coulomb	H Bond	NonBond	VdW	Coulomb	H Bond	NonBond	
	LYS 177	8.65	-171.98	-6.19	-169.52	0.20	-174.51	-3.33	-177.64	8.12
	LYS 175	1.59	-162.42	-4.93	-165.76	-2.60	-161.79	-0.16	-164.55	-1.22
	LYS 172	-0.28	-159.18	-0.78	-160.24	-1.62	-158.79	-0.63	-161.05	0.80
	LYS 163	6.54	-157.81	-4.80	-156.06	-1.33	-141.73	-0.02	-143.09	-12.98
	LYS 160	-1.22	-138.51	0.00	-139.73	3.52	-146.18	0.00	-142.67	2.94
	LYS 207	-0.03	-75.10	0.00	-75.13	-0.04	-75.73	0.00	-75.77	0.64
	ARG 209	-0.04	-71.55	0.00	-71.58	-0.05	-72.21	0.00	-72.25	0.67
Chain D	HSE 166	5.13	-14.03	-4.53	-13.43	-0.83	-6.97	0.00	-7.80	-5.63
	SER 214	-0.07	-5.85	0.00	-5.92	-0.10	-2.00	0.00	-2.09	-3.82
	VAL 174	-0.95	-3.15	0.00	-4.10	-1.09	-3.17	0.00	-4.26	0.17
	ILE 216	-0.31	-3.34	0.00	-3.64	-0.44	-3.31	0.00	-3.75	0.11
	VAL 168	-0.27	-2.77	0.00	-3.03	-0.33	-2.64	0.00	-2.97	-0.06
	VAL 208	-0.01	-0.83	0.00	-0.84	-0.02	-0.93	0.00	-0.94	0.10
	THR 212	-0.10	1.83	0.00	1.74	-0.13	0.41	0.00	0.28	1.46
	TYR 210	-0.01	1.78	0.00	1.77	-0.01	2.20	0.00	2.19	-0.41
	THR 173	-1.69	7.34	0.00	5.65	-1.89	3.99	0.00	2.10	3.56
	ASP 218	-0.06	83.76	0.00	83.70	-0.07	83.74	0.00	83.68	0.02

Table S3-12 – Per-residue energetic contributions in the Antithrombin-III/heparin analog predicted (left) and crystal (right) structures. [PDB: 1E03, res. 2.90 Å, RMSD: 0.60 Å].

	Residue	Docked				Crystal				$\Delta_{NonBond}$
		VdW	**Coulomb**	**H Bond**	**NonBond**	**VdW**	**Coulomb**	**H Bond**	**NonBond**	
	ARG 47	5.37	-206.85	-10.73	-212.21	5.88	-194.99	-4.73	-193.85	-18.36
	LYS 114	12.38	-211.46	-10.33	-209.40	-5.92	-219.34	-6.42	-231.68	22.28
	LYS 11	3.13	-202.41	-7.42	-206.70	-6.64	-175.36	0.00	-182.00	-24.70
	ARG 46	9.21	-187.90	-8.44	-187.12	0.31	-171.42	-1.86	-172.98	-14.15
	ARG 13	9.47	-177.67	-12.91	-181.11	-0.70	-117.01	-1.69	-119.39	-61.71
	LYS 125	-1.21	-134.22	0.00	-135.43	176.01	-192.82	-0.26	-17.07	-118.36
	ARG 129	4.95	-129.62	-8.03	-132.71	-0.61	-120.34	-2.08	-123.03	-9.68
	ARG 24	-0.29	-95.38	0.00	-95.67	-0.16	-99.79	0.00	-99.95	4.29
	ARG 132	-0.15	-93.62	0.00	-93.77	-0.36	-100.85	0.00	-101.21	7.44
	ASN 45	-2.51	-17.11	-5.46	-25.08	-4.27	-15.33	-4.67	-24.27	-0.81
	SER 112	-1.18	-11.59	0.00	-12.77	-1.47	1.62	0.00	0.16	-12.93
	PRO 12	-1.66	-8.21	0.00	-9.87	3.69	-10.49	0.00	-6.80	-3.07
Chain I	THR 44	-4.47	-3.49	0.00	-7.96	-2.79	0.12	0.00	-2.67	-5.29
	ALA 43	-3.12	-4.65	0.00	-7.77	-3.92	-1.74	0.00	-5.66	-2.12
	VAL 48	-1.15	-5.49	0.00	-6.64	0.26	-6.05	0.00	-5.79	-0.86
	PHE 122	-1.04	-1.68	0.00	-2.72	0.26	-1.98	0.00	-1.71	-1.01
	ILE 40	-0.40	-1.93	0.00	-2.33	-0.29	-2.29	0.00	-2.57	0.25
	PHE 121	-0.37	-1.23	0.00	-1.60	-0.72	-1.42	0.00	-2.14	0.54
	LEU 126	-0.17	-0.39	0.00	-0.56	-0.31	0.04	0.00	-0.27	-0.29
	LEU 417	-0.20	-0.32	0.00	-0.53	-0.24	-0.48	0.00	-0.72	0.20
	GLN 118	-0.23	0.24	0.00	0.01	-0.50	-4.03	0.00	-4.53	4.55
	THR 115	-0.42	0.54	0.00	0.12	-0.42	3.03	0.00	2.61	-2.49
	PRO 41	-0.26	5.91	0.00	5.65	-0.17	4.70	0.00	4.53	1.12
	GLU 42	-0.54	79.06	0.00	78.53	-0.39	89.43	0.00	89.04	-10.51
	GLU 113	1.90	92.68	-1.04	93.55	11.78	97.20	0.00	108.98	-15.43
	ASP 14	-0.11	107.49	0.00	107.38	-0.30	116.97	0.00	116.66	-9.29
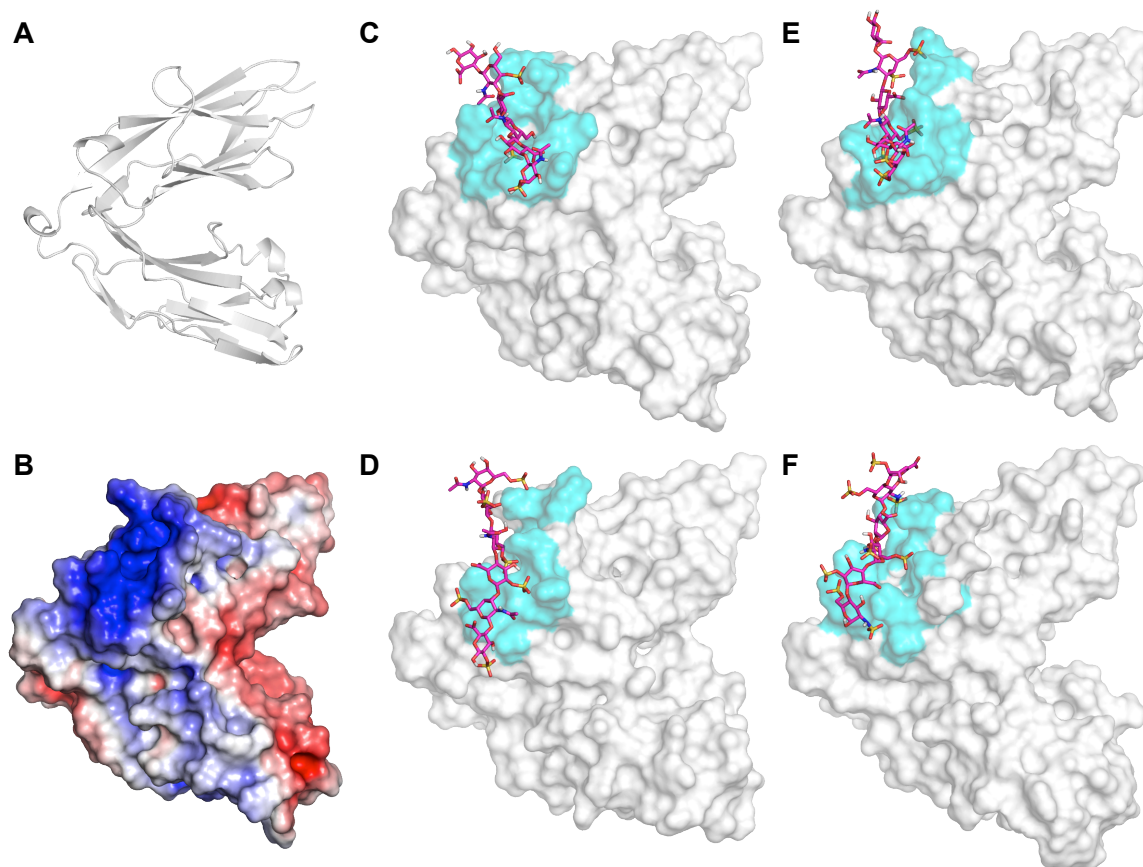
Figure S3-14 – RPTPσ. (A) Ig1 and Ig2 domains of RPTPσ. (B) Electrostatic potential surface. (C-F) Predicted structures of CS-A, CS-D, CS-E, and heparin after docking and molecular dynamics.
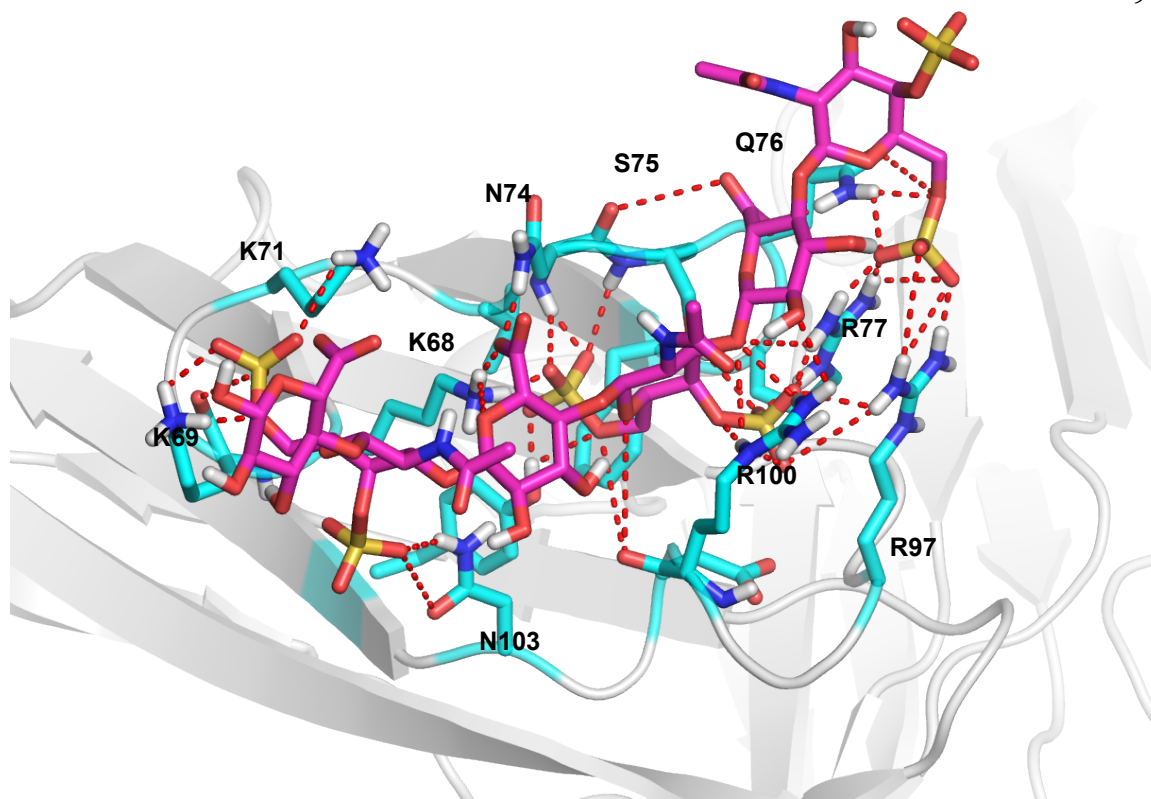
Figure S3-15 – Predicted structure of CS-E hexamer (magenta) bound to RPTPσ with 5 Å binding site shown (cyan). Dashed lines indicate hydrogen bonding and salt bridges between ligand and protein.
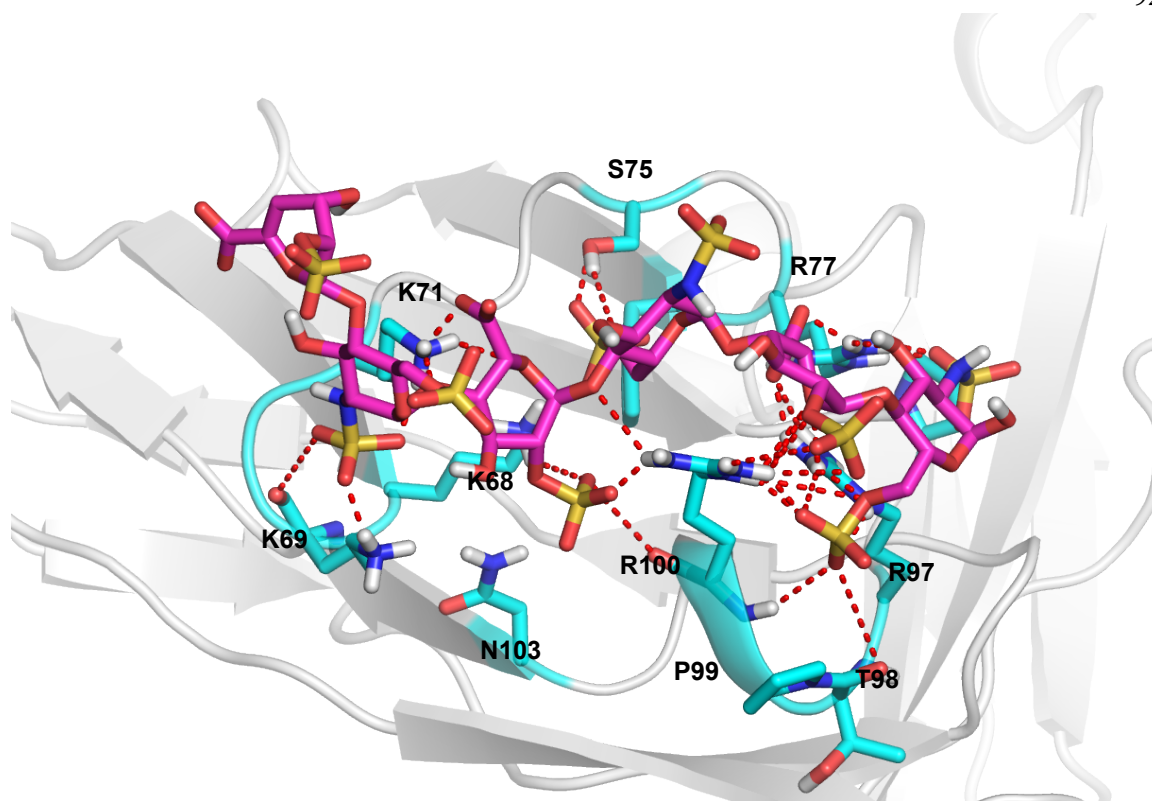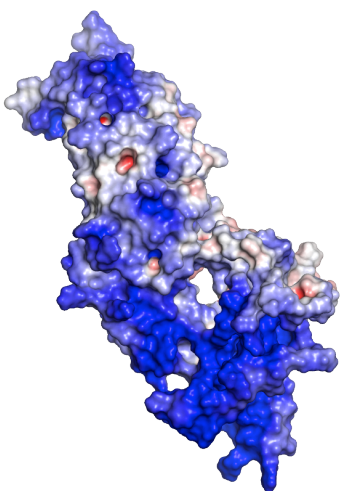
Figure S3-16 – Predicted structure of heparin hexamer (magenta) bound to RPTPσ with 5 Å binding site shown (cyan). Dashed lines indicate hydrogen bonding and salt bridges between ligand and protein.

Table S3-13 – Per-residue energetic contributions in the predicted RPTPσ/CS-A (left) and RPTPσ/CS-D (right) structures.

Residue	CS-A				CS-D			
	VdW	Coulomb	H Bond	NonBond	VdW	Coulomb	H Bond	NonBond
ARG 77	2.59	-109.82	-8.26	-115.50	2.85	-152.95	-10.80	-160.91
LYS 68	9.11	-108.48	-12.32	-111.69	-0.54	-100.52	0.00	-101.06
ARG 100	-2.41	-90.30	-2.04	-94.75	11.00	-174.16	-25.17	-188.33
ARG 97	9.71	-89.82	-11.85	-91.97	-0.68	-134.41	-4.42	-139.50
LYS 71	-1.67	-85.86	0.00	-87.54	14.25	-141.64	-11.80	-139.20
LYS 69	2.01	-99.90	-6.62	-104.51	-0.19	-76.14	0.00	-76.33
LYS 72	--	--	--	--	-0.46	-75.57	0.00	-76.03
GLN 76	-1.67	-7.74	-4.48	-13.89	1.86	-16.06	-8.45	-22.65
ASN 74	-0.86	2.13	0.00	1.27	-0.30	-0.29	-5.86	-6.45
SER 75	4.90	-12.36	-4.75	-12.21	-2.31	-6.93	0.00	-9.24
ASN 103	-1.20	-2.24	0.00	-3.44	-0.15	-1.06	0.00	-1.20
GLU 102	-0.23	48.03	0.00	47.80	--	--	--	--
GLY 70	--	--	--	--	--	--	--	--
PRO 95	--	--	--	--	-1.05	1.32	0.00	0.27
PRO 99	--	--	--	--	--	--	--	--
THR 98	--	--	--	--	-0.19	1.83	0.00	1.65
VAL 73	-0.82	-2.94	0.00	-3.77	-0.30	-1.35	0.00	-1.65
TYR 105	--	--	--	--	-0.09	-2.46	0.00	-2.55
PHE 78	-3.66	-1.37	0.00	-5.03	--	--	--	--
ASP 101	-0.63	75.50	0.00	74.88	--	--	--	--

Table S3-14 – Per-residue energetic contributions in the predicted RPTPσ/CS-E (left) and RPTPσ/heparin (right) structures.

Residue	CS-E				heparin			
	VdW	Coulomb	H Bond	NonBond	VdW	Coulomb	H Bond	NonBond
ARG 77	11.74	-158.46	-17.21	-163.92	0.89	-180.82	-7.26	-187.18
LYS 68	10.98	-158.86	-10.24	-158.12	-0.60	-170.34	-1.68	-172.61
ARG 100	-0.66	-139.54	-9.43	-149.63	3.44	-208.70	-9.97	-215.23
ARG 97	1.84	-137.33	-5.15	-140.64	2.01	-180.78	-8.27	-187.04
LYS 71	-2.11	-131.74	0.00	-133.86	4.10	-223.34	-3.40	-222.65
LYS 69	3.46	-115.00	-5.67	-117.21	-1.69	-127.16	0.00	-128.85
LYS 72	-0.37	-65.91	0.00	-66.28	--	--	--	--
GLN 76	5.83	-20.07	-12.97	-27.22	-0.17	-5.26	0.00	-5.43
ASN 74	2.57	-15.72	-10.33	-23.48	-0.22	-1.46	0.00	-1.68
SER 75	-1.95	-10.28	-0.59	-12.83	-0.85	-7.68	-0.18	-8.71
ASN 103	-1.49	-9.18	0.00	-10.67	-0.26	-9.19	0.00	-9.45
GLU 102	--	--	--	--	--	--	--	--
GLY 70	--	--	--	--	-0.15	0.74	0.00	0.59
PRO 95	--	--	--	--	-0.54	4.62	0.00	4.08
PRO 99	--	--	--	--	-1.04	-2.44	0.00	-3.47
THR 98	--	--	--	--	-0.28	3.73	0.00	3.45
VAL 73	-2.38	-5.93	0.00	-8.31	--	--	--	--
TYR 105	3.55	-6.81	-4.76	-8.02	--	--	--	--
PHE 78	-3.37	1.18	0.00	-2.19	-1.31	-0.46	0.00	-1.77
ASP 101	-1.75	97.79	0.00	96.04	--	--	--	--
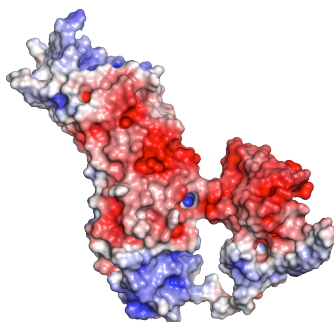
A – NgR1   **B – NgR2**   **C – NgR3**
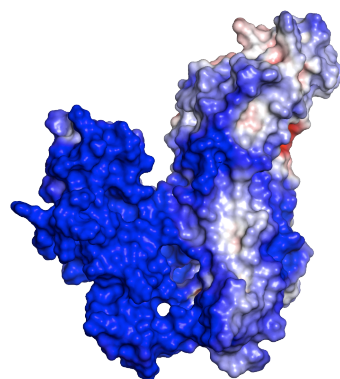
Figure S3-17 – Electrostatic potential surfaces of (A) NgR1, (B) NgR2, and (C) NgR3. Note the lack of positive charge on NgR2, but strong positive charge on NgR1 and NgR3.
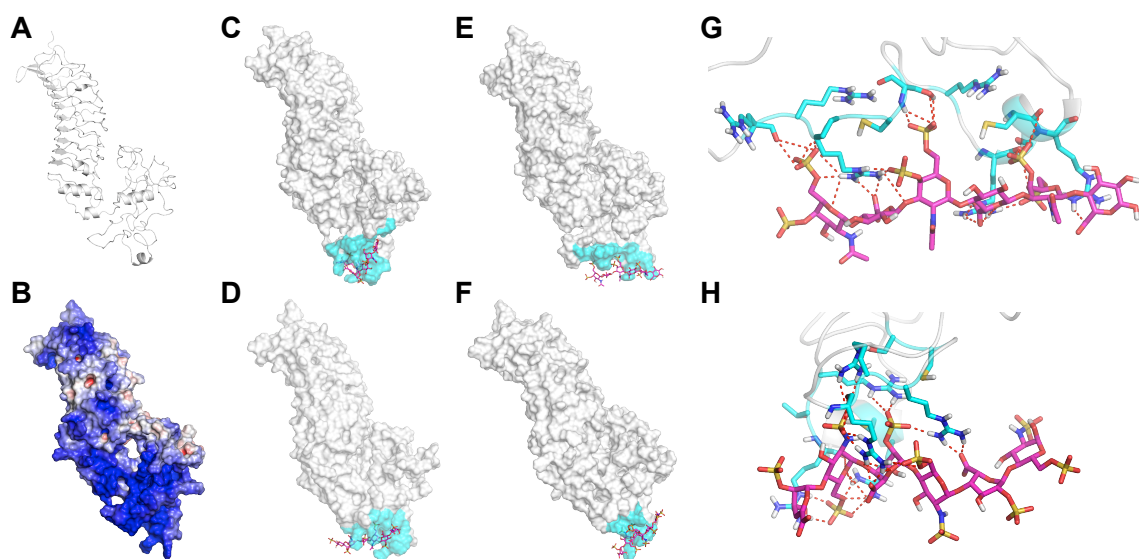
Figure S3-18 – NgR1. (A) Structure of NgR1. (B) Electrostatic potential surface showing strong positive charge. (C-F) Predicted structures of CS-A, CS-D, CS-E, and heparin after docking and molecular dynamics. (G-H) Detailed view of CS-E and heparin predicted structures.
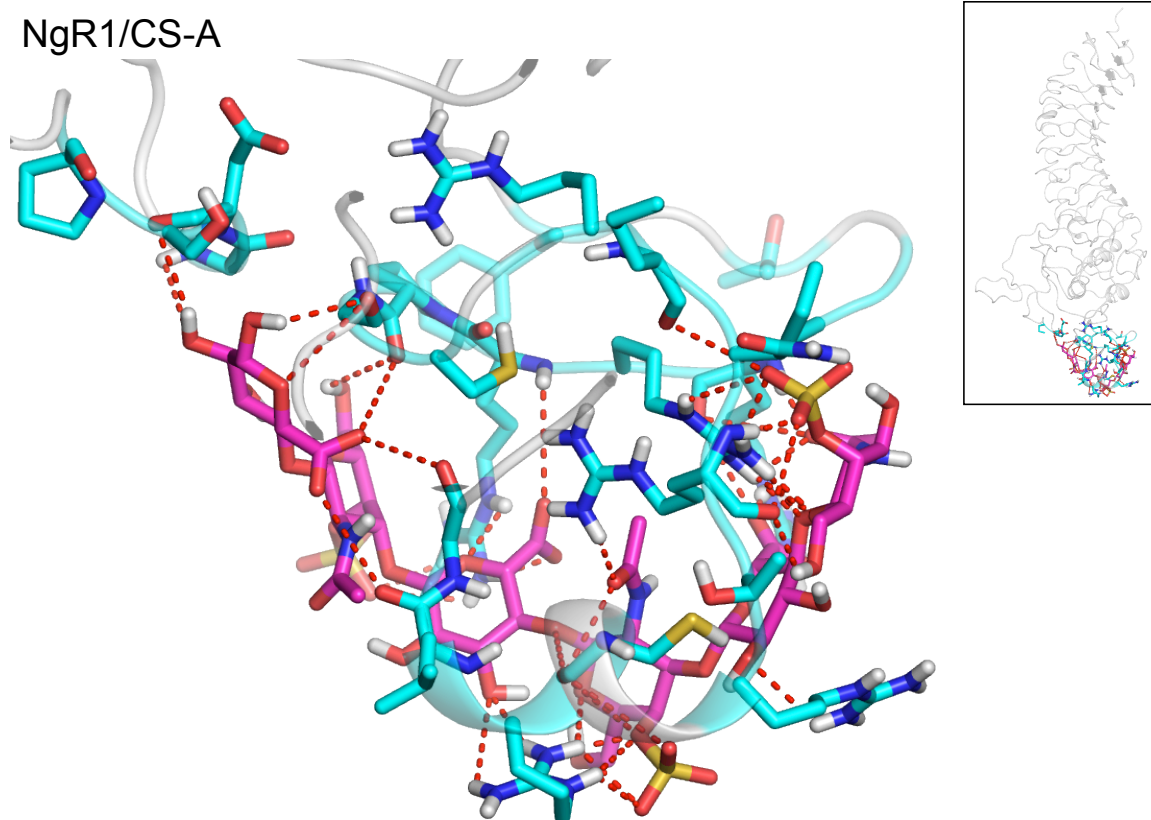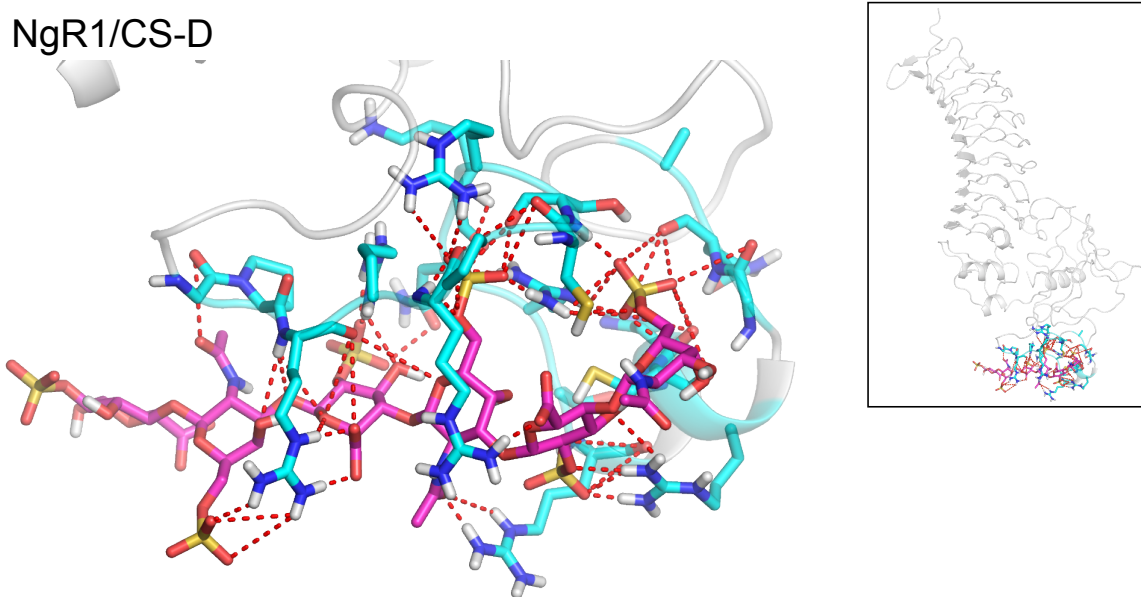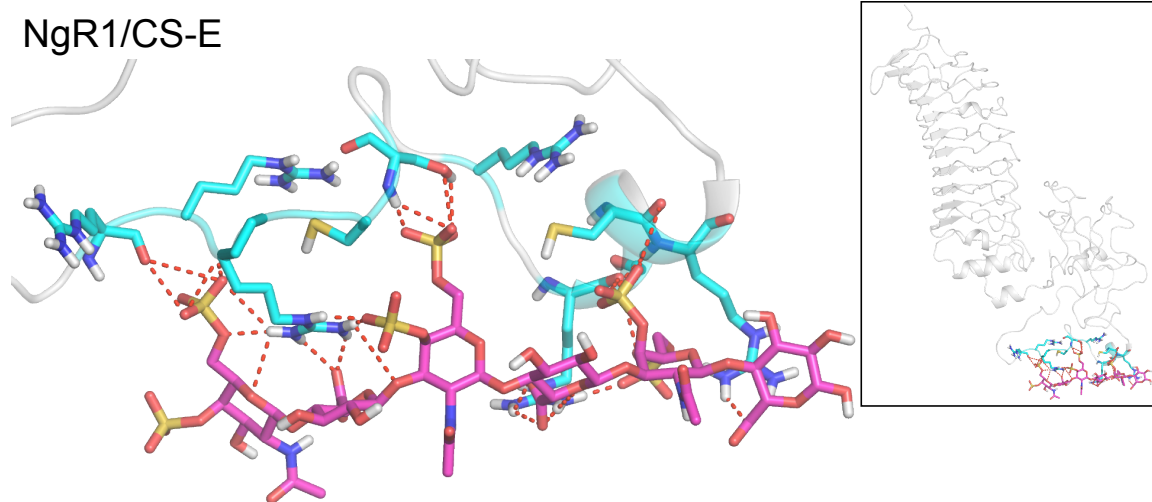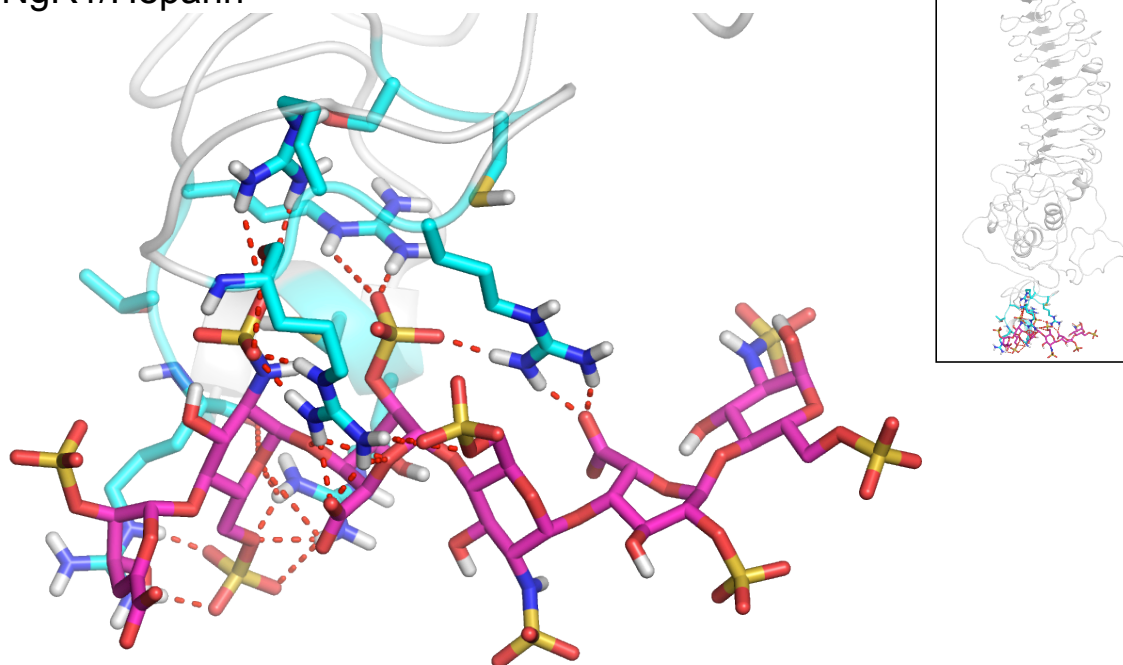
NgR1/CS-A

Figure S3-19 – Detail of predicted NgR1/CS-A structure after docking and dynamics with CS-A hexamer (magenta) and 5 Å binding site (cyan) shown. Dashed lines indicate hydrogen bonding and salt bridges between ligand and protein. Overall placement on protein shown in inset.

NgR1/CS-D

Figure S3-20 – Detail of predicted NgR1/CS-D structure after docking and dynamics with CS-D hexamer (magenta) and 5 Å binding site (cyan) shown. Dashed lines indicate hydrogen bonding and salt bridges between ligand and protein.

NgR1/CS-E

Figure S3-21 – Detail of predicted NgR1/CS-E structure after docking and dynamics with CS-E hexamer (magenta) and 5 Å binding site (cyan) shown. Dashed lines indicate hydrogen bonding and salt bridges between ligand and protein.

NgR1/Heparin

Figure S3-22 – Detail of predicted NgR1/heparin structure after docking and dynamics with heparin hexamer (magenta) and 5 Å binding site (cyan) shown. Dashed lines indicate hydrogen bonding and salt bridges between ligand and protein.

Table S3-15 – Per-residue energetic contributions in the predicted NgR1 structures for CS-A, CS-D, CS-E, and heparin.

| Residue		CS-A				CS-D				CS-E				Heparin			
		VdW	Coulomb	H Bond	NonBond	VdW	Coulomb	H Bond	NonBond	VdW	Coulomb	H Bond	NonBond	VdW	Coulomb	H Bond	NonBond
ARG	390	6.94	-90.88	-13.23	-97.17	2.15	-136.95	-11.48	-146.28	-1.11	-61.48	0.00	-62.59	5.12	-213.83	-16.07	-224.78
ARG	392	-2.73	-107.51	-5.79	-116.04	-2.26	-126.71	-8.96	-137.93	-0.19	-158.71	-14.92	-173.82	2.77	-191.60	-10.23	-199.06
ARG	406	-2.67	-96.20	-7.45	-106.33	4.79	-116.69	-8.19	-120.09	2.55	-131.51	-12.53	-141.50	-1.21	-176.87	-6.87	-184.95
ARG	402	-3.57	-69.97	0.00	-73.53	0.76	-120.34	-4.53	-124.10	3.02	-147.77	-12.85	-157.59	0.82	-151.54	-9.09	-159.81
ARG	400	-0.48	-96.72	-5.19	-102.39	8.97	-144.72	-15.76	-151.51	-0.73	-98.90	0.00	-99.63	4.04	-142.10	-5.53	-143.59
ARG	391	-2.06	-111.17	-8.33	-121.56	1.17	-142.38	-7.89	-149.09	-1.38	-105.45	0.00	-106.83	-1.06	-134.39	0.00	-135.44
ARG	397	-0.25	-56.79	0.00	-57.04	-1.74	-101.89	-0.03	-103.66	-0.15	-72.85	0.00	-73.00	-0.06	-96.30	0.00	-96.36
LYS	398	-0.40	-40.49	0.00	-40.89	-0.78	-81.71	0.00	-82.49	-0.14	-58.40	0.00	-58.54	-0.06	-68.64	0.00	-68.70
PRO	389	-4.08	-5.91	0.00	-9.99	-4.13	-4.22	0.00	-8.34	-0.33	-3.98	0.00	-4.31	-0.36	-4.12	0.00	-4.48
GLY	408	-1.82	-0.24	0.00	-2.06	-0.81	-5.51	0.00	-6.32	-0.09	-4.24	0.00	-4.33	-0.07	-4.17	0.00	-4.24
GLY	388	-0.62	-3.62	0.00	-4.24	-0.96	-6.68	0.00	-7.64	-0.04	-3.15	0.00	-3.19	-0.03	-4.10	0.00	-4.13
CYS	405	-1.71	0.31	-2.35	-3.75	-0.20	-5.66	-2.02	-7.88	-0.01	-8.79	0.00	-8.80	-3.89	-0.16	0.00	-4.05
ASN	399	-1.35	-5.54	0.00	-6.89	-1.93	1.27	0.00	-0.65	-0.19	-4.50	0.00	-4.70	-0.31	-3.64	0.00	-3.95
PHE	384	-0.69	-1.25	0.00	-1.94	-0.23	-2.07	0.00	-2.30	-0.03	-1.51	0.00	-1.55	-0.07	-2.90	0.00	-2.97
LEU	407	-0.98	0.71	0.00	-0.27	-0.25	-1.87	0.00	-2.12	-0.27	-1.86	0.00	-2.14	-0.07	-1.97	0.00	-2.04
GLY	394	1.03	-2.84	0.00	-1.81	-0.56	0.65	0.00	0.09	-0.50	0.68	0.00	0.18	-0.05	-1.33	0.00	-1.38
CYS	395	-2.02	-1.44	0.00	-3.46	-0.43	-9.15	0.00	-9.58	-2.79	-12.58	0.00	-15.37	-0.65	-0.26	0.00	-0.91
SER	344	-0.83	-0.23	0.00	-1.07	-0.11	-0.55	0.00	-0.66	-0.01	-1.48	0.00	-1.49	-0.02	-0.19	0.00	-0.21
THR	444	0.00	-0.53	0.00	-0.53	-0.01	1.78	0.00	1.78	0.00	-0.46	0.00	-0.46	0.00	0.64	0.00	0.64
ALA	410	-0.17	-0.76	0.00	-0.93	-0.24	0.61	0.00	0.37	-0.02	-0.05	0.00	-0.07	-0.03	1.06	0.00	1.03
THR	386	-0.20	0.59	0.00	0.39	-0.06	1.06	0.00	1.00	-0.01	1.22	0.00	1.21	-0.01	1.16	0.00	1.15
HSE	404	-0.48	1.27	0.00	0.79	-0.60	2.33	0.00	1.73	-0.29	0.25	0.00	-0.04	-0.23	1.87	0.00	1.63
GLN	409	-0.49	1.79	0.00	1.30	-1.17	9.18	0.00	8.01	-0.07	3.92	0.00	3.85	-0.07	2.02	0.00	1.95
PRO	345	-0.13	0.77	0.00	0.64	-0.04	1.85	0.00	1.82	0.00	1.29	0.00	1.29	-0.01	2.08	0.00	2.08
GLY	342	-0.99	-1.11	0.00	-2.10	-0.04	2.58	0.00	2.55	-0.01	1.93	0.00	1.93	-0.02	2.20	0.00	2.18
THR	401	-0.66	2.74	0.00	2.08	-0.46	4.98	0.00	4.52	-0.37	3.92	0.00	3.55	-0.72	3.17	0.00	2.45
SER	396	-0.18	3.43	0.00	3.25	0.59	5.47	-3.85	2.21	3.30	-2.21	-4.89	-3.80	-0.18	2.69	0.00	2.51
PRO	393	-3.03	4.64	0.00	1.61	-0.79	7.05	0.00	6.26	-0.40	7.33	0.00	6.92	-0.24	5.85	0.00	5.61
SER	403	-0.18	3.43	0.00	3.25	-0.19	2.81	0.00	2.61	-1.02	1.80	0.00	0.78	-0.35	6.34	0.00	5.99
ASP	343	-1.62	48.13	0.00	46.51	-0.07	71.82	0.00	71.74	-0.01	61.99	0.00	61.98	-0.02	82.58	0.00	82.56
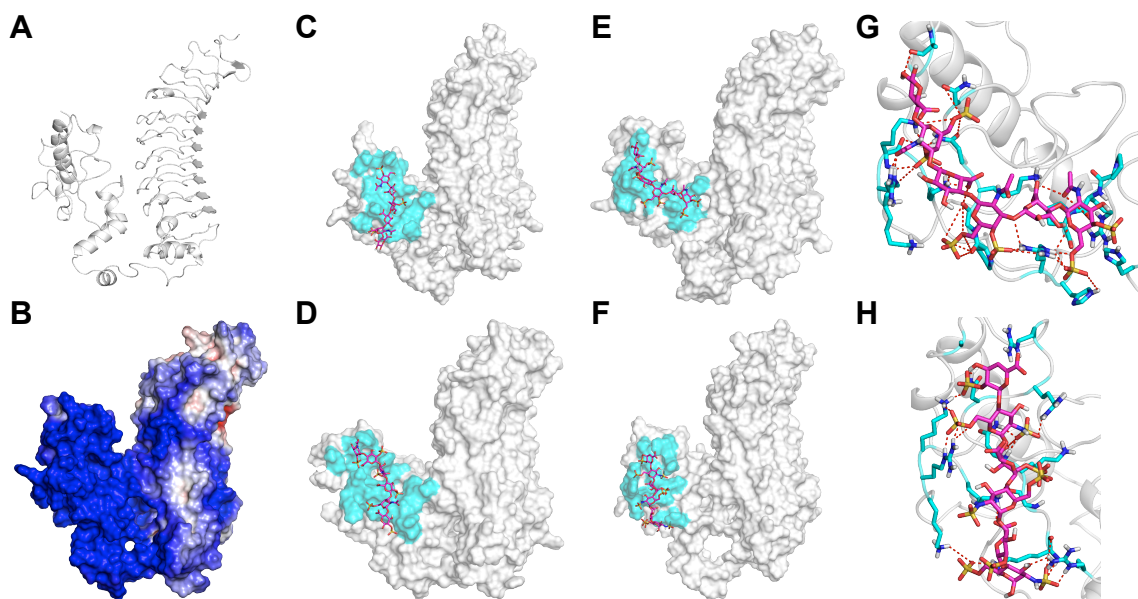
Figure S3-23 – NgR3. (A) Structure of NgR3. (B) Electrostatic potential surface. (C-F) Predicted structures of CS-A, CS-D, CS-E, and heparin after docking and molecular dynamics. (G-H) Detailed view of CS-E and heparin predicted structures.
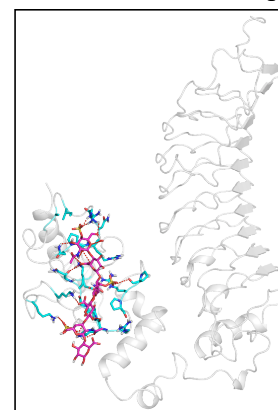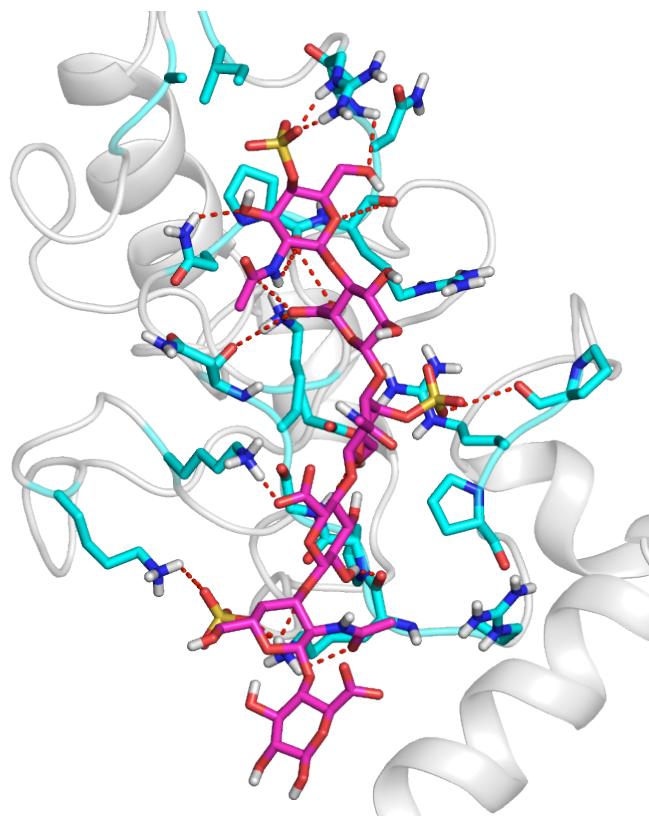
NgR3/CS-A

Figure S3-24 – Detail of predicted NgR3/CS-A structure after docking and dynamics with CS-A hexamer (magenta) and 5 Å binding site (cyan) shown. Dashed lines indicate hydrogen bonding and salt bridges between ligand and protein.
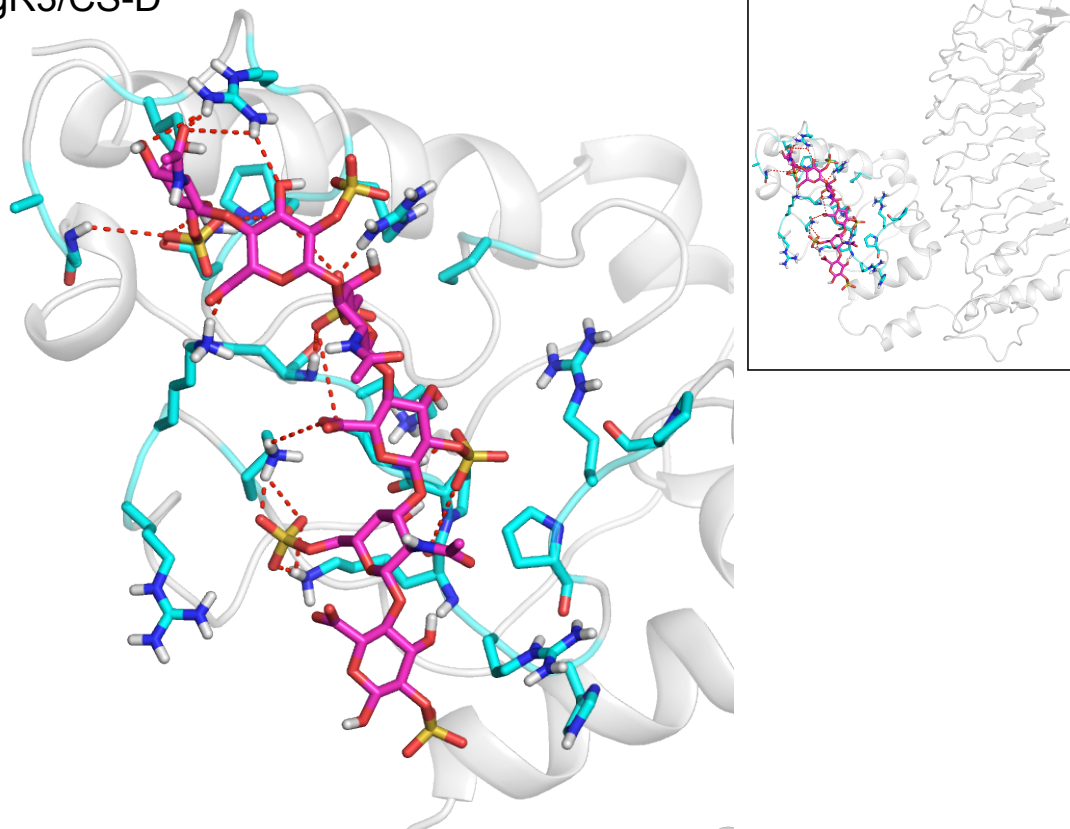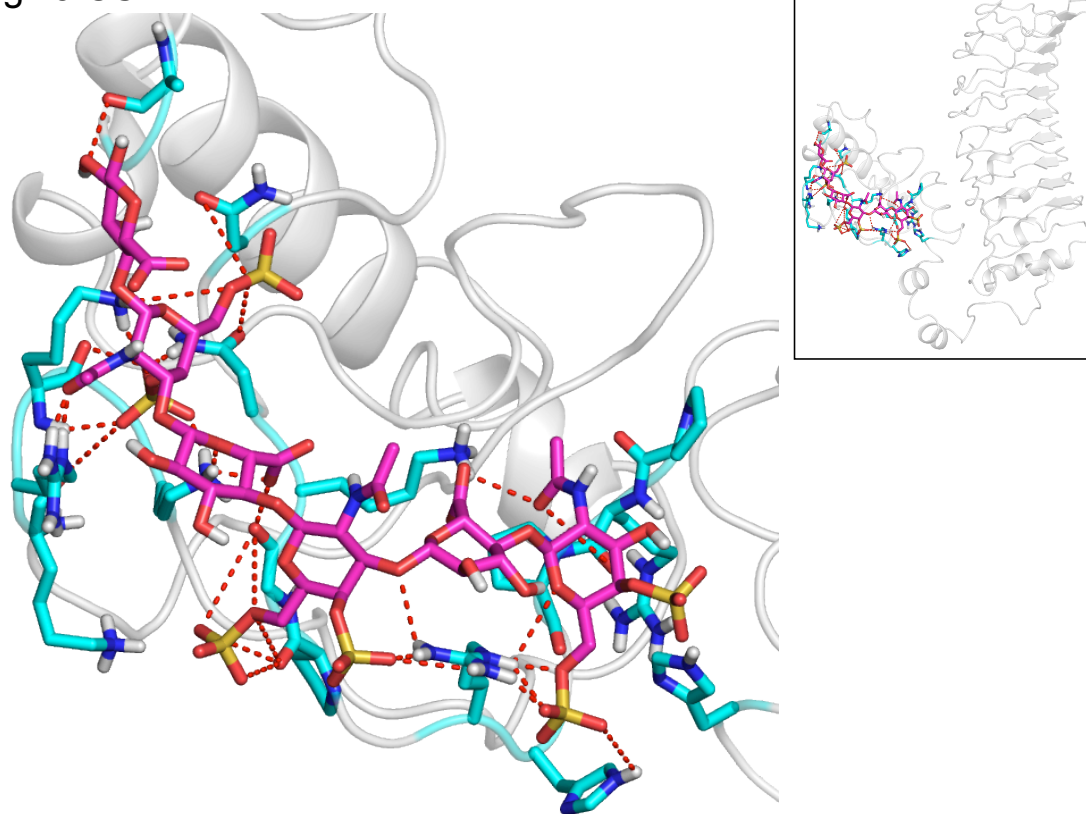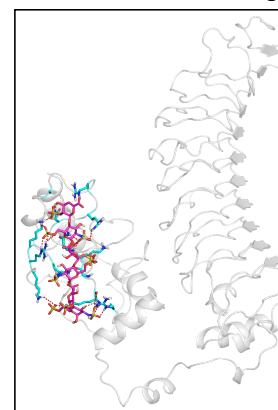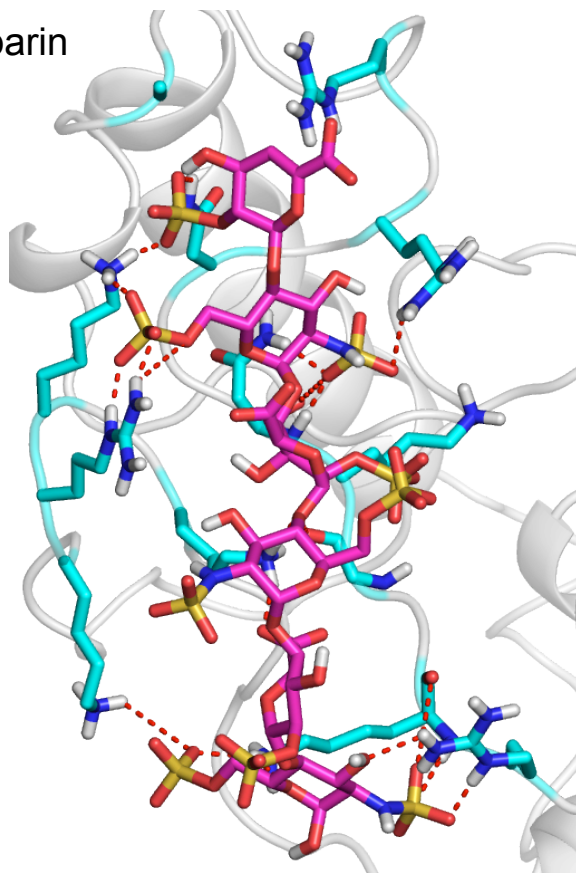
NgR3/CS-D

Figure S3-25 – Detail of predicted NgR3/CS-D structure after docking and dynamics with CS-D hexamer (magenta) and 5 Å binding site (cyan) shown. Dashed lines indicate hydrogen bonding and salt bridges between ligand and protein.

NgR3/CS-E

Figure S3-26 – Detail of predicted NgR3/CS-E structure after docking and dynamics with CS-E hexamer (magenta) and 5 Å binding site (cyan) shown. Dashed lines indicate hydrogen bonding and salt bridges between ligand and protein.

NgR3/Heparin

Figure S3-27 – Detail of predicted NgR3/heparin structure after docking and dynamics with heparin hexamer (magenta) and 5 Å binding site (cyan) shown. Dashed lines indicate hydrogen bonding and salt bridges between ligand and protein.

Table S3-16 – Per-residue energetic contributions in the predicted NgR3 structures for CS-A, CS-D, CS-E, and heparin.

Residue		CS-A				CS-D				CS-E				Heparin			
		VdW	Coulomb	H Bond	NonBond	VdW	Coulomb	H Bond	NonBond	VdW	Coulomb	H Bond	NonBond	VdW	Coulomb	H Bond	NonBond
LYS	383	4.11	-102.12	-2.70	-100.71	0.45	-152.91	-4.15	-156.61	6.52	-162.33	-9.44	-165.24	7.58	-206.62	-11.23	-210.27
ARG	380	-0.04	-40.12	0.00	-40.16	-1.06	-102.20	0.00	-103.26	-1.20	-119.85	-5.80	-126.85	3.48	-182.45	-7.59	-186.56
LYS	381	-0.17	-52.67	0.00	-52.84	0.75	-138.39	-4.12	-141.76	4.02	-139.02	-10.71	-145.71	7.81	-180.38	-6.68	-179.25
ARG	330	-0.84	-63.93	0.00	-64.77	-2.80	-102.67	0.00	-105.47	-0.31	-153.39	-11.01	-164.70	2.79	-158.26	-5.44	-160.90
ARG	340	-2.65	-68.57	0.00	-71.22	1.84	-118.19	-5.24	-121.59	-0.29	-83.03	0.00	-83.32	-1.34	-156.72	-2.65	-160.71
LYS	331	-0.27	-98.70	-4.75	-103.72	3.13	-123.36	-5.79	-126.02	-0.63	-74.84	0.00	-75.48	-0.71	-153.93	-0.76	-155.40
LYS	334	-1.13	-89.69	-4.68	-95.50	-2.39	-97.83	0.00	-100.22	-2.53	-141.48	-1.46	-145.47	-3.30	-134.35	0.00	-137.65
LYS	379	-0.84	-81.40	-0.02	-82.25	-0.17	-67.58	0.00	-67.74	-0.37	-84.61	0.00	-84.99	-1.05	-130.60	0.00	-131.66
ARG	342	2.01	-72.80	-6.37	-77.17	-2.08	-104.32	-3.28	-109.68	-0.09	-68.84	0.00	-68.93	-0.81	-118.99	0.00	-119.80
ARG	326	-1.18	-62.89	0.00	-64.07	-0.84	-92.99	0.00	-93.83	-2.41	-72.84	0.00	-75.25	-0.08	-97.25	0.00	-97.33
ASN	335	-1.84	0.07	0.00	-1.77	2.32	-9.47	-4.60	-11.75	-1.99	-9.78	-3.64	-15.41	-0.19	-12.30	-6.78	-19.27
ASN	338	-1.39	-2.82	-0.16	-4.37	-1.61	-2.72	-0.08	-4.41	-1.12	-2.24	0.00	-3.37	-1.17	-3.49	0.00	-4.66
PRO	362	-0.25	-0.75	0.00	-1.00	-0.20	-2.05	0.00	-2.25	-0.02	-1.54	0.00	-1.57	-0.02	-2.42	0.00	-2.44
PRO	327	-0.88	-3.14	0.00	-4.01	-0.87	-3.83	0.00	-4.70	-3.57	0.38	0.00	-3.18	-0.22	-1.95	0.00	-2.17
GLY	333	0.34	-0.67	-4.29	-4.63	-1.59	-1.25	-3.92	-6.77	-2.38	4.27	0.00	1.89	-1.51	-0.23	0.00	-1.74
GLY	382	-0.09	0.75	0.00	0.66	-0.12	2.17	0.00	2.05	-1.28	1.34	0.00	0.06	-0.25	-1.36	0.00	-1.61
ILE	345	-0.85	-0.11	0.00	-0.96	-1.88	-0.42	0.00	-2.30	-0.12	-0.55	0.00	-0.67	-0.08	-0.78	0.00	-0.86
ALA	350	-0.30	-2.38	0.00	-2.68	-0.12	-1.27	0.00	-1.39	-0.13	-0.71	0.00	-0.84	-0.02	-0.79	0.00	-0.81
ASN	341	-1.36	0.73	0.00	-0.63	-0.15	2.42	0.00	2.27	-0.04	0.79	0.00	0.75	-0.06	0.00	0.00	-0.07
GLY	349	-0.16	-2.75	0.00	-2.91	-0.45	-4.02	0.00	-4.47	-1.21	-2.14	0.00	-3.35	-0.06	0.43	0.00	0.37
PRO	332	-2.68	-0.11	0.00	-2.79	-1.95	-2.37	0.00	-4.32	-0.92	4.48	0.00	3.55	-0.59	1.27	0.00	0.68
PRO	339	-4.19	5.10	0.00	0.92	-0.55	8.20	0.00	7.65	-0.28	5.86	0.00	5.59	-0.26	1.69	0.00	1.43
ALA	348	-0.46	-3.28	0.00	-3.74	-0.29	-2.64	0.00	-2.93	-1.34	-2.64	0.00	-3.97	-0.44	2.12	0.00	1.69
HSE	309	-0.02	-0.37	0.00	-0.40	-0.02	0.60	0.00	0.58	-0.65	-1.57	0.00	-2.21	-0.02	1.89	0.00	1.87
HSE	329	-0.06	0.65	0.00	0.58	-0.27	0.00	0.00	-0.26	-1.25	-1.38	0.00	-2.63	-0.26	3.43	0.00	3.18
PRO	325	-0.44	3.13	0.00	2.69	-0.19	3.21	0.00	3.03	-2.53	-1.17	0.00	-3.70	-0.03	3.36	0.00	3.33
ASP	359	-0.30	64.07	0.00	63.78	-0.04	79.36	0.00	79.32	-0.03	69.11	0.00	69.09	-0.08	100.87	0.00	100.79

Table S3-17 – Single residue mutation data for RPTPs. Values show change in binding energy (kcal/mol) relative to wildtype structures. Values are shown both for the change in hydrogen bonding for the specific mutated residue as well as the overall change in the full cavity binding energy. The cavity binding energy is further separated into hydrogen bonding + van der Waals or Coulomb energy.

PTPS Increased Binding																		
PTPS Residue			Per-Res ΔHBond				CSA Cavity			CSD Cavity			CSE Cavity			HEP Cavity		
num	from	to	CSA	CSD	CSE	HEP	ΔCav	Δ(HB+VDW)	ΔCou	ΔCav	Δ(HB+VDW)	ΔCou	ΔCav	Δ(HB+VDW)	ΔCou	ΔCav	Δ(HB+VDW)	ΔCou
73	V	N	-1.48	0.00	-6.17	0.00	1.56	-6.53	8.09	5.03	7.96	-2.93	-28.66	3.08	-31.75	-1.41	-2.47	1.07
73	V	Q	-1.82	0.00	0.00	0.00	-2.36	-5.15	2.78	-3.85	5.70	-9.56	-32.20	-6.47	-25.73	-5.87	-0.20	-5.66
74	N	Q	0.00	-4.29	5.91	0.00	-11.00	-3.44	-7.56	13.75	1.60	12.14	14.66	10.45	4.21	2.97	-3.06	6.03
75	S	N	-1.22	-4.66	-1.17	0.31	-7.17	7.22	-14.40	-35.76	-4.34	-31.41	11.00	1.23	9.78	24.41	0.73	23.69
75	S	Q	4.75	-1.11	4.44	0.31	26.31	29.85	-3.54	-28.87	-6.92	-21.96	21.53	24.46	-2.94	21.00	2.33	18.68
76	Q	N	-1.61	1.19	-1.50	0.00	-9.37	-2.33	-7.04	0.44	-0.59	1.02	2.28	5.24	-2.97	6.07	-1.82	7.89
78	F	N	-4.58	0.00	0.00	0.00	3.34	0.46	2.89	5.48	5.98	-0.50	-3.23	3.50	-6.73	6.58	1.98	4.60
78	F	Q	0.00	0.00	-3.07	0.00	-11.05	-4.91	-6.15	-8.99	4.79	-13.79	-6.42	6.54	-12.97	2.47	-2.04	4.51
103	N	Q	-1.14	0.00	5.15	-0.04	-13.39	-0.59	-12.80	-22.49	-8.02	-14.47	-6.56	0.38	-6.94	-6.77	-3.88	-2.88

PTPS Decreased Binding																		
PTPS Residue			Per-Res ΔHBond				CSA Cavity			CSD Cavity			CSE Cavity			HEP Cavity		
num	from	to	CSA	CSD	CSE	HEP	ΔCav	Δ(HB+VDW)	ΔCou	ΔCav	Δ(HB+VDW)	ΔCou	ΔCav	Δ(HB+VDW)	ΔCou	ΔCav	Δ(HB+VDW)	ΔCou
68	K	N	7.58	0.00	5.88	9.87	95.67	8.45	87.22	79.75	-5.99	85.73	119.99	-3.28	123.26	137.68	1.17	136.51
68	K	Q	7.60	0.00	0.43	9.87	103.11	7.80	95.31	77.89	-4.12	82.01	116.16	-0.89	117.05	160.96	3.13	157.83
69	K	N	8.27	0.00	-0.43	0.41	109.55	12.56	96.99	87.95	5.61	82.35	84.90	-3.08	87.97	123.59	-1.29	124.88
69	K	Q	8.27	0.00	5.12	0.41	97.91	5.28	92.63	75.40	4.98	70.41	90.73	-5.27	95.99	135.29	-6.80	142.10
71	K	N	4.58	4.29	1.68	5.71	78.37	4.92	73.44	84.49	-3.90	88.39	74.38	-1.00	75.38	172.64	-0.70	173.34
71	K	Q	6.15	-2.56	0.20	11.24	89.01	13.20	75.81	74.24	-11.41	85.65	72.17	-1.89	74.06	185.03	13.95	171.08
77	R	Q	6.96	6.37	6.84	14.14	100.48	5.10	95.38	128.38	3.40	124.98	107.04	-9.98	117.03	163.36	0.66	162.70
77	R	N	7.01	0.96	11.82	14.14	94.89	2.33	92.57	130.30	-1.43	131.72	108.53	-10.16	118.69	165.41	0.61	164.81
97	R	N	4.59	9.78	-0.96	12.05	100.76	0.66	100.09	123.99	1.22	122.76	121.08	11.91	109.17	189.16	-0.56	189.72
97	R	Q	4.59	9.78	-0.05	6.35	91.62	-0.55	92.18	116.85	2.75	114.09	114.11	1.33	112.78	188.49	0.66	187.84
100	R	N	12.01	18.70	3.81	15.24	98.76	2.89	95.88	150.09	5.51	144.58	139.31	0.52	138.79	219.62	-1.39	221.02
100	R	Q	12.01	23.01	0.71	15.53	91.91	2.23	89.69	132.35	2.97	129.37	112.37	3.65	108.72	221.74	1.56	220.19

Table S3-18 – Single residue mutation data for NgR1. Values show change in binding energy (kcal/mol) relative to wildtype structures. Values are shown both for the change in hydrogen bonding for the specific mutated residue as well as the overall change in the full cavity binding energy. The cavity binding energy is further separated into hydrogen bonding + van der Waals or Coulomb energy.

NGR1 Increased Binding																		
NGR1 Residue			Per-Res ΔHBond				CSA Cavity			CSD Cavity			CSE Cavity			HEP Cavity		
num	from	to	CSA	CSD	CSE	HEP	ΔCav	Δ(HB+VDW)	ΔCou	ΔCav	Δ(HB+VDW)	ΔCou	ΔCav	Δ(HB+VDW)	ΔCou	ΔCav	Δ(HB+VDW)	ΔCou
395	C	Q	-5.33	0.00	-4.87	0.00	-7.24	2.09	-9.33	3.60	-1.74	5.34	8.95	0.38	8.57	6.30	-3.63	9.93
396	S	N	0.00	-1.73	-6.06	0.00	-3.19	3.57	-6.76	-15.44	-3.64	-11.80	9.88	3.95	5.93	10.94	-3.36	14.31
396	S	Q	0.00	4.38	-0.05	-4.85	-6.51	3.69	-10.21	-0.97	1.83	-2.81	15.97	5.70	10.27	-13.35	-5.15	-8.19
399	N	Q	4.67	-3.26	0.00	0.00	2.86	2.29	0.58	-7.57	-2.71	-4.86	2.18	-0.67	2.85	-47.06	-1.26	-45.80
403	S	Q	0.00	0.00	-5.22	0.00	4.39	4.40	0.00	-3.76	-2.31	-1.45	5.82	2.99	2.84	-1.31	-4.93	3.62
405	C	N	-6.52	-4.36	-0.79	-3.27	-8.64	5.99	-14.62	-24.39	-5.79	-18.61	-0.64	-0.16	-0.47	-0.03	-7.67	7.65
405	C	Q	0.00	-1.60	-6.10	0.00	-4.76	8.05	-12.81	-4.87	5.03	-9.90	-3.39	-0.36	-3.04	-0.92	-5.56	4.64

NGR1 Decreased Binding																		
NGR1 Residue			Per-Res ΔHBond				CSA Cavity			CSD Cavity			CSE Cavity			HEP Cavity		
num	from	to	CSA	CSD	CSE	HEP	ΔCav	Δ(HB+VDW)	ΔCou	ΔCav	Δ(HB+VDW)	ΔCou	ΔCav	Δ(HB+VDW)	ΔCou	ΔCav	Δ(HB+VDW)	ΔCou
390	R	Q	0.86	8.12	0.00	14.17	83.82	3.55	80.28	127.85	4.00	123.84	74.90	-2.34	77.24	216.92	-6.24	223.17
390	R	N	3.65	7.85	0.00	20.17	91.45	4.43	87.03	129.28	7.46	121.83	103.46	1.07	102.40	214.66	5.94	208.73
391	R	N	12.39	1.33	4.80	0.00	111.02	12.01	99.03	117.11	-3.64	120.74	133.74	3.22	130.51	104.52	-5.12	109.65
391	R	Q	12.39	5.69	4.80	0.00	81.87	1.91	79.96	108.81	6.44	102.37	130.43	2.71	127.72	116.57	-6.14	122.71
392	R	N	5.47	-0.86	10.62	6.61	87.18	6.33	80.86	120.25	11.02	109.24	165.18	11.93	153.25	176.91	4.80	172.12
392	R	Q	5.93	-0.64	10.64	7.72	88.87	5.06	83.81	111.70	3.80	107.91	165.48	10.73	154.75	175.74	3.43	172.31
400	R	N	0.88	15.38	0.00	5.59	75.35	3.35	72.00	140.99	10.79	130.20	95.87	-1.00	96.87	141.97	-4.20	146.17
400	R	Q	0.95	11.95	0.00	5.57	88.95	9.99	78.97	135.65	8.85	126.80	93.43	-0.12	93.56	108.39	-2.58	110.97
402	R	Q	7.41	5.08	12.90	4.13	78.45	8.42	70.03	107.96	-4.30	112.26	147.99	4.21	143.78	142.76	-4.02	146.78
402	R	N	7.47	6.67	0.70	2.92	84.77	9.26	75.52	110.69	-4.12	114.81	144.72	3.64	141.08	149.66	-3.21	152.87
406	R	Q	6.16	2.32	13.46	5.97	91.65	9.39	82.27	86.91	-5.04	91.95	136.94	2.12	134.82	167.79	2.68	165.11
406	R	N	7.34	4.44	12.49	5.97	103.23	11.66	91.57	97.02	3.78	93.24	135.69	1.72	133.98	181.99	-1.47	183.46

Table S3-19 – Single residue mutation data for NgR3. Values show change in binding energy (kcal/mol) relative to wildtype structures. Values are shown both for the change in hydrogen bonding for the specific mutated residue as well as the overall change in the full cavity binding energy. The cavity binding energy is further separated into hydrogen bonding + van der Waals or Coulomb energy.

NGR3 Increased Binding																			
NGR3 Residue			Per-Res ΔHBond				CSA Cavity			CSD Cavity			CSE Cavity			HEP Cavity		
num	from	to	CSA	CSD	CSE	HEP	ΔCav	Δ(HB+VDW)	ΔCou	ΔCav	Δ(HB+VDW)	ΔCou	ΔCav	Δ(HB+VDW)	ΔCou	ΔCav	Δ(HB+VDW)	ΔCou
338	N	Q	1.43	0.06	3.53	-5.31	-4.84	2.39	-7.23	6.70	0.74	5.96	18.28	-2.09	20.37	0.10	1.74	-1.64
345	I	Q	-4.24	-5.59	0.00	0.00	-3.12	-0.93	-2.20	0.80	-3.97	4.78	-10.18	-7.76	-2.41	-0.10	-0.19	0.08
348	A	N	-4.60	0.00	-0.78	-2.15	-12.91	-2.87	-10.04	-5.07	-2.65	-2.42	-5.76	-1.24	-4.51	-12.19	-3.71	-8.48

NGR3 Decreased Binding																			
NGR3 Residue			Per-Res ΔHBond				CSA Cavity			CSD Cavity			CSE Cavity			HEP Cavity		
num	from	to	CSA	CSD	CSE	HEP	ΔCav	Δ(HB+VDW)	ΔCou	ΔCav	Δ(HB+VDW)	ΔCou	ΔCav	Δ(HB+VDW)	ΔCou	ΔCav	Δ(HB+VDW)	ΔCou
330	R	N	0.74	-1.09	9.03	0.08	84.09	9.33	74.77	49.41	-4.51	53.92	149.89	2.24	147.65	125.52	-3.79	129.32
330	R	Q	0.74	-2.10	7.54	-0.17	84.81	10.32	74.49	28.03	-5.77	33.80	152.89	2.27	150.63	127.01	-5.33	132.33
331	K	Q	4.31	5.31	1.87	-2.08	92.34	0.99	91.35	25.97	-7.63	33.60	105.28	6.51	98.78	155.28	-2.14	157.42
331	K	N	7.53	5.75	1.87	-6.82	101.31	7.32	94.00	31.23	-5.72	36.95	100.70	6.15	94.55	148.88	-1.89	150.77
334	K	N	2.01	-6.09	9.00	0.00	70.93	-2.08	73.02	70.93	-6.27	77.20	154.48	-2.05	156.53	119.55	-2.40	121.96
334	K	Q	6.57	0.00	3.57	0.00	53.70	1.07	52.63	93.72	-3.94	97.67	102.98	-2.46	105.44	130.15	-0.69	130.84
340	R	N	0.00	-1.29	0.00	5.17	64.44	1.69	62.74	117.17	-4.79	121.96	73.59	-5.51	79.09	112.55	-10.32	122.87
340	R	Q	0.00	-1.28	0.00	5.17	64.45	0.34	64.11	72.83	-7.89	80.72	77.98	-11.87	89.85	120.72	-7.44	128.16
342	R	N	8.86	16.64	5.66	0.00	71.30	4.52	66.77	128.14	0.11	128.03	95.01	-5.88	100.89	108.88	-8.34	117.22
342	R	Q	8.86	16.07	5.66	0.00	63.84	3.86	59.98	126.70	-0.15	126.85	92.95	-4.70	97.65	108.36	-6.29	114.65
379	K	N	0.00	0.00	0.00	5.58	3.64	-4.34	7.99	76.86	-2.33	79.19	82.12	-1.28	83.39	158.63	2.23	156.40
379	K	Q	0.00	0.00	0.00	5.58	11.27	2.03	9.24	72.12	-1.96	74.08	84.91	-0.05	84.96	158.55	-1.94	160.48
380	R	N	0.00	5.43	0.59	3.93	42.61	-0.06	42.68	51.23	0.39	50.85	66.95	-3.91	70.86	188.74	-3.93	192.67
380	R	Q	0.00	5.43	2.81	1.21	35.33	0.26	35.08	45.62	-0.61	46.23	69.83	-10.08	79.91	196.39	-3.00	199.40
381	K	N	0.00	4.69	8.58	1.68	56.14	2.87	53.27	84.96	-2.92	87.89	119.97	-5.89	125.86	146.31	-14.85	161.17
381	K	Q	0.00	4.69	8.27	-7.65	47.50	0.85	46.65	110.48	-0.09	110.57	120.14	-4.00	124.14	137.24	-17.81	155.05
383	K	Q	-5.14	6.10	2.09	6.77	42.26	2.69	39.58	63.75	-7.34	71.09	95.05	-3.91	98.96	154.07	-9.80	163.87
383	K	N	0.00	6.10	10.92	7.95	42.16	1.41	40.75	60.25	-2.41	62.66	92.99	-2.73	95.71	176.79	-5.68	182.47

List of Figures

List of Tables